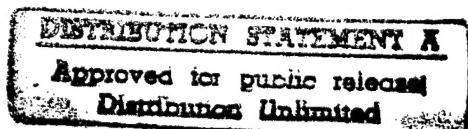


Columbia University
in the City of New York

HARMONIC MILLIMETER RADIATION FROM A MICROWAVE FREE ELECTRON LASER AMPLIFIER

Yan-Hua Liu



1997



19970613 036

DTIC QUALITY INSPECTED 3

Work Supported by ONR Grant N00014-96-1-1136

Plasma Physics Laboratory

Department of Applied Physics

School of Engineering and Applied Science

Columbia University

New York, New York 10027

REPORT DOCUMENTATION PAGE			Form Approved OMB No. 0704-0188	
Public reporting burden for this collection of information is estimated to average 1 hour per response, including the time for reviewing instructions, searching existing data sources, gathering and maintaining the data needed, and completing and reviewing the collection of information. Send comments regarding this burden estimate or any other aspect of this collection of information, including suggestions for reducing this burden, to Washington Headquarters Services, Directorate for Information Operations and Reports, 1215 Jefferson Davis Highway, Suite 1204, Arlington, VA 22202-4302, and to the Office of Management and Budget, Paperwork Reduction Project (0704-0188), Washington, DC 20503.				
1. AGENCY USE ONLY (Leave blank)	2. REPORT DATE June 1997	3. REPORT TYPE AND DATES COVERED Technical		
4. TITLE AND SUBTITLE Harmonic Millimeter Radiation from a Microwave Free Electron Laser Amplifier		5. FUNDING NUMBERS G N00014-96-1-1136		
6. AUTHOR(S) Yan-Hua Liu				
7. PERFORMING ORGANIZATION NAME(S) AND ADDRESS(ES) Columbia University Department of Applied Physics 500 W. 120th St., New York, NY 10027		8. PERFORMING ORGANIZATION REPORT NUMBER Plasma Lab Report 132		
9. SPONSORING/MONITORING AGENCY NAME(S) AND ADDRESS(ES) Office of Naval Research Arlington, VA 22217		10. SPONSORING/MONITORING AGENCY REPORT NUMBER		
11. SUPPLEMENTARY NOTES To be published in Physical Review E				
12a. DISTRIBUTION/AVAILABILITY STATEMENT Unlimited		12b. DISTRIBUTION CODE		
13. ABSTRACT (Maximum 200 words)				

In this project an electron beam is bunched at a microwave frequency and the harmonics of this bunching drive radiation at millimeter wavelengths, using a FEL configured as a single-pass travelling wave amplifier. A 10kW 24GHz microwave input signal grows to ~200kW level using the lower frequency unstable root of the waveguide FEL dispersion relation. The Columbia FEL facility operates at this frequency in the TE₁₁ mode, using a helical undulator (1.85cm period) and a 3mm dia. 600kV electron beam contained in a 8.7mm ID cylindrical waveguide. The harmonic currents set up by the microwave are found to cause growth of harmonic power under two conditions. When the upper frequency root corresponds to the third harmonic, we observe a small amount of third harmonic emission in the TE₁₁ mode, accompanied by comparable second harmonic. The millimeter harmonic radiation produced is coherent and phase-related to the microwave source. Second, we have found substantial emission at the seventh harmonic, most likely in the TE₇₂ mode-- which in cylindrical waveguide travels at very nearly the same wave speed as the 24GHz power. In order to excite the seventh harmonic radiation, the electron beam must be displaced from the system axis ~2mm in this device. We present a theoretical model of the experiment which predicts that if the microwave signal is strong enough to drive the FEL into saturation, the harmonic radiation becomes powerful.

14. SUBJECT TERMS Free Electron Laser, Millimeter Waves, Harmonic Radiation, Coherent Radiation Source			15. NUMBER OF PAGES 88
			16. PRICE CODE
17. SECURITY CLASSIFICATION OF REPORT Unclassified	18. SECURITY CLASSIFICATION OF THIS PAGE Unclassified	19. SECURITY CLASSIFICATION OF ABSTRACT Unclassified	20. LIMITATION OF ABSTRACT

HARMONIC MILLIMETER RADIATION FROM A
MICROWAVE FREE ELECTRON LASER AMPLIFIER

Yan-Hua Liu

Submitted in partial fulfillment of the
requirements for the degree
of Doctor of Philosophy
in the Graduate School of Arts and Science

COLUMBIA UNIVERSITY

1997

DTIC QUALITY INSPECTED 3

© 1997

Yan-Hua Liu

All Rights Reserved

Abstract

Harmonic Millimeter Radiation From a Microwave Free Electron Laser Amplifier

Yan-Hua Liu

Experimental and theoretical studies of harmonic millimeter radiation have been carried out with the Columbia free electron laser (FEL) operated as a single-pass traveling wave amplifier. We have caused bunching of electrons in a beam produced by the amplification of a coherent microwave source to drive appreciable harmonic radiation at millimeter wavelengths. A 10kW 24GHz microwave input signal grows to ~400kW level by using the lower frequency unstable root of the waveguide FEL dispersion relation. The FEL operates at this frequency in the TE_{11} mode, using a helical undulator (1.85cm period) and a 3mm diameter 600kV electron beam contained in a 8.7mm ID cylindrical waveguide.

We found experimental evidence for two types of harmonic production. First, we choose the parameters of the device so that the upper frequency root of the FEL dispersion corresponds to the third harmonic, in which case we observed a small amount (a few hundred watts) of third harmonic emission, accompanied by comparable second harmonic. The experiment also shows that the millimeter harmonic radiation produced is coherent and phase-related to the microwave bunching source. Secondly, we have found kW level emission for the first time at the seventh harmonic, most likely from the TE_{72} mode, in which case the seventh harmonic happens to travel at very nearly the same wave speed as the 24GHz TE_{11} wave in the cylindrical waveguide. In order to excite the seventh harmonic

radiation, the electron beam has to be displaced from the system axis, $\sim 2\text{mm}$ in our case. The seventh harmonic output is potentially an attractive choice for a CW FEL which must generate appreciable power at $\sim 2\text{mm}$ wavelength for plasma electron cyclotron heating since we can produce this radiation for electron beam energy as low as 400kV . In both cases, the experiments show that no harmonic power is produced without gain and substantial power output at the fundamental.

We also developed a one-dimensional theoretical model of the experiment. Numerical methods were used to integrate the complete set of first-order partial differential FEL equations, which describe the coupling between the two harmonically related waves and the electron beam. The computational results are consistent with our experimental observations. From the numerical study we find that if the microwave input signal is strong enough to drive the FEL into saturation, the harmonic radiation should become more powerful.

Table of Contents

Abstract	
Acknowledgment	
Chapter 1	Introduction
	Reference
Chapter 2	Theory and FEL Equations.....
2.1	The Basic FEL Theory
2.1.1	The Basic FEL Equations
2.2	The FEL Resonant Harmonic Conversion Theory
2.2.1	The Compton Waveguide FEL Equation with Slippage
2.2.2	The Two Resonant Waves in the Waveguide FEL
2.2.3	The Two Resonant Waves Compton Model
2.3	The 7th Harmonic Co-generation Theory
2.3.1	Co-generation Group Velocity Matching
2.3.2	The 2-wave Model for the 7th Harmonic Co-generation
2.4	The Two-wave Raman Model
	Reference
Chapter 3	Experimental Apparatus
3.1	Electron Beam Generation
3.1.1	Marx Capacitor Bank
3.1.2	Pulse Forming Line
3.1.3	Vaccum Diode
3.2	FEL Interaction
3.2.1	The Solenoid
3.2.2	FEL Assembly.....

3.2.3 Constant Period Undulator	36
3.3 FEL Diagnostics	40
3.3.1 Detectors and Oscilloscopes	41
3.3.2 Diffraction Grating Spectrometer	43
3.3.3 Harmonic Frequency Coherence Experimental Setup	43
Reference	46
Chapter 4 Experimental Results	47
4.1 The FEL Resonant Harmonic Conversion Experimental Results	47
4.1.1 Experimental Design	47
4.1.2 The Power Calibration	50
4.1.3 The Amplification of the 24GHz wave	51
4.1.4 The Observation of the Harmonic Radiations	52
4.1.5 The Harmonic Frequency Coherence Experiment.....	55
4.2 The Observation of the Seventh Harmonic Emission	57
4.3 The Oscillator Experiments	61
4.4 The current wave-form and its effects	62
Reference	62
Chapter 5 Numerical Model and Simulation Results	63
5.1 The Numerical Model for the 2-wave Compton FEL	63
5.2 Simulation Results Related to the Third Harmonic	66
5.3 Simulation Results Related to the 7th Harmonic Co-generation	73
5.4 The Single-Frequency Code	78
Reference	80
Chapter 6 Conclusion	81

Chapter 1

Introduction

The term "Free Electron Laser" (FEL) was used by Madey [1] in 1977 to describe an electron beam device he constructed at Stanford University [2,3] which could amplify radiation at optical wavelengths. This source of radiation was developed by Motz and others [4,5] about two decades earlier, but advances in accelerator technology allowed Madey to extend the operating range of the FEL into the Infrared. The FEL operates by using an relativistic electron beam to amplify radiation via stimulated emission. The source of the radiation is that the FEL process causes an orderly bunching of the electron beam, and these bunches, when properly phased, result in coherent high power radiation.

A typical FEL has three components: an electron accelerator that generates the high-intensity, low-emittance relativistic electron beam; a wiggler or undulator that provides a periodic static transverse magnetic field to wiggler the electron trajectory; and resonator cavity that permits feedback of the radiation signal. Fig. 1.1 shows the schematic of a free electron laser with a linearly polarized wiggler composed of individual permanent magnets. As shown in the figure, when the relativistic electron beam passes along the axis (the z-axis) of the wiggler, the magnetic field of the wiggler (in the y-direction) bends the electron motion and gives it a sinusoidal transverse velocity in the x-direction (v_x). Under the presence of a radiation wave that is polarized in the y-direction and propagating along z-direction, there is a Lorentz force $-ev_x \times B_y$ acting on the electron beam in the z-direction. This force (ponderomotive force) bunches the electron beam, and it is this bunching that changes the uniform spacing of the electrons and permits a coherent, continuous exchange of energy between the electrons and the radiation wave. Under the "resonance condition":

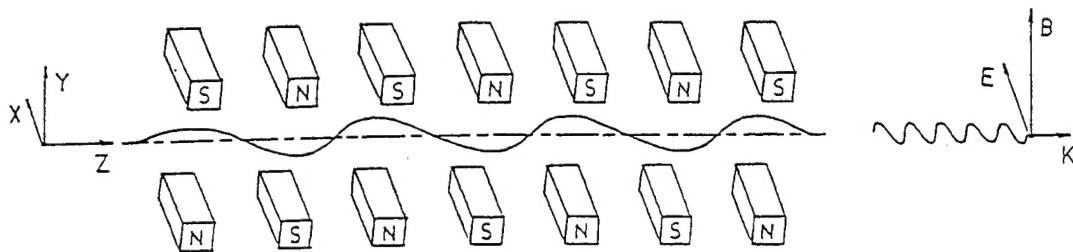


Fig. 1.1 Schematic of a free electron laser with a linearly polarized wiggler.

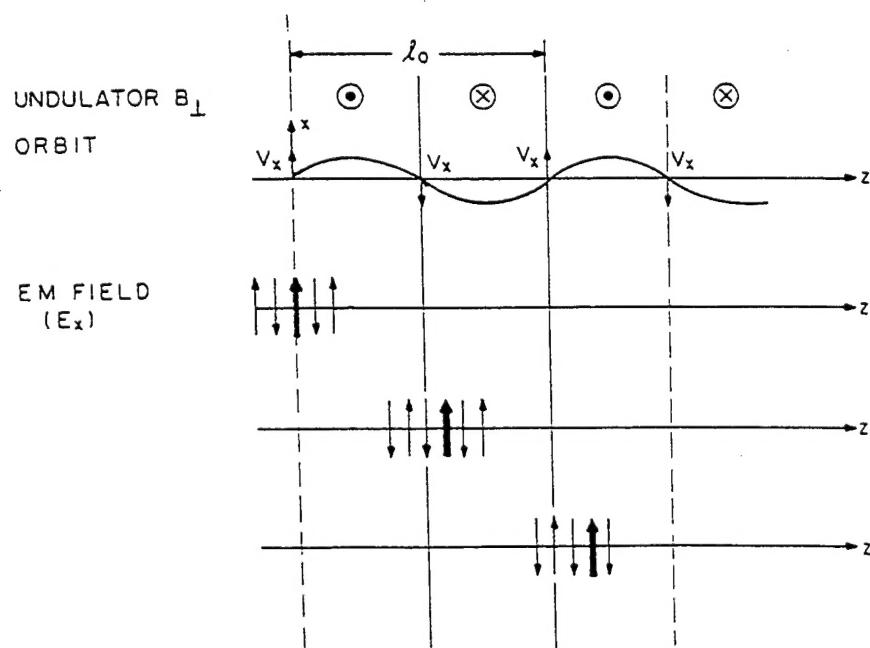


Fig. 1.2 Relation between radiation and electron motion in resonance condition; the undulator field is shown above. The boldface arrow in the field is a reference. (after Morton, [6])

for each wiggler period the electrons transit, the radiation wave moves ahead of the electrons by one radiation wavelength (see Fig. 1.2), as shown in this figure, the radiation wave is always in phase with the electrons, so the radiation from the electron bunches can add up coherently.

Depending on the parameters of operations, FELs can be roughly classified into two categories: Compton FELs and Raman FELs. A Compton FEL involves a two wave Compton scattering process. In the frame that moves with the axial motion of the electron (the beam frame), the undulator magnetic field becomes an incoming EM wave. The undulator wave is back scattered by the electron beam and adds coherently to the signal wave under the resonance condition. We define $\tau_w = l_w / v_{\parallel}$, where l_w is the wiggler period and v_{\parallel} is the electron's axial velocity, as the time that the electrons travel one wiggler period, then the radiation will travel $c\tau_w$ distance at this same period of time. According to previous paragraph, the resonance condition can be expressed as :

$$c\tau_w = l_w + \lambda_s \quad (1.1)$$

where λ_s is the radiation wavelength. If one define $a_w / \gamma = v_{\perp} / v_{\parallel}$, where γ and v_{\perp} are the electron energy and transverse velocity respectively, it can be shown that $a_w = eB_w / k_w mc^2$ is the normalized vector potential of the wiggler with magnetic field strength B_w . From Eq.(1.1), we can deduce the radiation signal wavelength for a Compton FEL:

$$\lambda_s \approx \frac{l_w}{2\gamma^2} = \frac{1+a_w^2}{2\gamma^2} l_w \quad (1.2)$$

where $\gamma_{\parallel}^2 = \left(1 - \frac{v_{\parallel}^2}{c^2}\right)^{-1}$, $\gamma^2 = \left(1 - \frac{v_{\parallel}^2}{c^2} - \frac{v_{\perp}^2}{c^2}\right)^{-1}$ and $\gamma_{\perp}^2 = \frac{\gamma^2}{1+a_w^2}$.

When the interaction between electrons, namely the space-charge effect is not negligible, the FELs operate in the Raman regime, which involves a three wave Raman scattering process. The space-charge effect excites a plasma wave on the electron beam. In the beam frame, the undulator wave scatters off the plasma idler wave, giving part of its

energy to the plasma wave [7] and part to the emitted signal wave. The radiation signal frequency for a Raman FEL which includes the scattering off the "plasmon" with invariant plasma frequency $\omega_p = \sqrt{4\pi ne^2/\gamma m}$ is:

$$\omega_s = \frac{2\gamma^2}{1+a_w^2} \left(\omega_w - \frac{\omega_p c}{\gamma v_1} \right) \quad (1.3)$$

where n is the electron beam density and $\omega_w = 2\pi c/l_w$. The space-charge effect downshifts the effective undulator period: $2\pi/l_{w(Raman)} = 2\pi/l_{w(Compton)} + \omega_p/\gamma v_1$.

In the past, considerable attention has been devoted to developing harmonic radiations in an FEL device [8], in order to get shorter wavelength for a given electron beam energy. This is of great advantage for FELs which operate with energy less than 1MV, where one might wish to generate radiations at 0.5-2.0mm wavelength for the purpose of plasma ECR heating. A reduction of energy by a factor of two or more would permit a much less expensive technology to be used for the production of CW FEL energy. Earlier works [8,9] show that FEL oscillators could produce harmonic radiation, though the level is orders of magnitude less than the fundamental. The cause of this phenomenon is that the primary FEL interaction results in a bunched beam, and the bunching has many Fourier harmonic contents, which cause the harmonically related wave to grow. However, lacking some resonant or phase-matching process, even though the amplitudes of these harmonic components of the electron bunching fall off slowly with the harmonic number, the energy converted from the fundamental to the harmonic is quite small [10]. Some FELs, which have a "dipole wiggler" (as shown in Fig. 1.1) naturally have gain at the third harmonic, and such a device has been successfully operated and produced radiation in the near UV [11].

In this thesis, we explore harmonic operation in a microwave Raman FEL. Our motivation is not just to produce harmonic radiation in the shorter wavelength, i.e. the millimeter spectrum, which can be done easily in an oscillator configuration based on the

mechanism we described in the previous paragraph. Our objective is to operate the FEL as a traveling wave amplifier, and use a coherent source wave which is obtained from a commercial 24GHz magnetron to prebunch the electron beam in order to generate frequency and phase related harmonic radiation for the application in which a stable phase and frequency relationship between the harmonic radiation is required, such as in the pulse radar.

The virtues of prebunching an electron beam undergoing FEL interaction in an undulator have been described many times in the past [12,13], but experiments have been few [14,15,16] thus far. If the electron beam is prebunched by a coherent source, then radiation at the harmonics will also be coherent, and the harmonic radiation should be related in phase and frequency to the source which bunches the electron beam. Appreciable harmonic power depends on gain at the FEL harmonic [11], or some mechanism to couple energy from the microwave FEL frequency into the harmonic.

Recently, Piovella et al [17] have studied a waveguide FEL where the beam is bunched by a growing wave at the low frequency beam wave intersection, prompting growth at a harmonically-related high frequency upper intersection, or FEL mode; a similar idea was also described by Sternbach[18]. In a waveguide FEL, there are two unstable roots of the dispersion relation, which represent the two growing waves. By injecting a small signal at low frequency, a strong signal and bunching are produced at the high frequency. The advantage of this mechanism is that the low frequency source is an existing intense coherent source of microwave which is readily available, i.e., the 24GHz magnetron signal. The FEL harmonic output is then in the millimeter spectrum, and we can expect it to relate to the stable frequency and phase of the microwave source. It should be possible to reach saturated output of the high frequency wave in a single pass, avoiding the use of a multi-pass resonator; one would then obtain a stable output frequency free of the sidebands which can result from an oscillator configuration. Growth of both waves is

exponential under conditions of relatively low electron beam energy and high current density. We call this mechanism "FEL resonant harmonic conversion".

More recently, Wang et al [19] have introduced a new harmonic radiation mechanism, called "co-generation". This mechanism is based on the fact that certain TE_{s1} electromagnetic modes of a cylindrical waveguide at frequency $s\omega$ exhibit coincidental near matching between their wave velocities and that of the TE_{11} mode at frequency ω . This basic characteristic of the simplest closed guided wave structure may allow the excitation of strong s -th harmonic radiation when a fundamental injected wave interacts with a nonlinear medium in the waveguide. Velocity matching can make the classical parametric interaction occur [20], and it may also allow a coupling in which the nonlinear medium supplies or receives significant power to or from the waves. The nonlinear medium here is the relativistic electron beam, and the lowest mode for which a near match in group velocity obtains is the TE_{72} at the seventh harmonic. We can expect the coherent radiation to be generated at the 7th harmonic.

In this thesis, we study an example of each mechanism, obtain experimental data which support the concept, and interpret these results with the aid of a theory that provides numerical output. First we present the harmonic radiation FEL theory: the FEL resonant harmonic conversion, the co-generation and the set of FEL equations with slippage for electron dynamics and two interacting waves which describes the coupling between the harmonically related waves. Chapter 3 is the detailed description of the Columbia FEL facility which we used to conduct the experiments. Then we show the experimental results: the growth of the low frequency bunching wave, the harmonic output based on the resonant harmonic conversion and the 7th harmonic co-generation. In Chapter 5 we present the numerical simulation of the experiments by numerically solving the set of FEL equations we deduced in Chapter 2. The discussion and conclusion are presented at the end of the thesis.

References:

- [1] J.M. Madey, *J. Appl. Phys.* **42**, p1906 (1971).
- [2] L.R. Elias, W.M. Fairbank, J.M.J. Madey, H.A. Schwettman, and T.I. Smith, *Phys. Rev. Lett.* **36**, p710 (1976).
- [3] D.A.G. Deacon, L.R. Elias, J.M.J. Madey, G.J. Ramian, H.A. Schwettman and T.I. Smith, *Phys. Rev. Lett.* **38**, p892 (1977).
- [4] H. Motz, W. Thon, and R.M. Whitehurst, *J. Appl. Phys.* **24**, p826 (1953).
- [5] M. Phillips, *IRE Trans. Elect. Dev.* **ED-7**, p231 (1960).
- [6] P.L. Morton, *Phys. Quan. Elect.*, **8**, p1 (1982).
- [7] T.C. Marshall, *Free Electron Lasers* (Macmillan Publishing Co., New York, 1985)
- [8] D.J. Bamford and D.A.G. Deacon, *Phys. Rev. Lett.* **62(10)**, p1106 (1989).
- [9] S. Benson, D.A.G. Deacon, J.N. Eckstein, J.M.J. Madey, K. Robinson, T.I. Smith and R. Taber, *J. Phys. (Paris) Coll.* **44**, C1-353 (1983).
- [10] Y. -P. Chou and T.C. Marshall, *Nucl. Instrum. Meth. in Phys. Res.* **A318**, p528 (1992).
- [11] P.G. O'Shea et al, *Nucl. Instrum. Meth. in Phys. Res.* **A341**, p7 (1994).
- [12] F. de Martini, review chapter in "*Laser Handbook, Volumn 6, Free Electron Lasers*", p195, ed. W.B. Colson, C. Pellegrini, and A. Renieri, N. Holland (1990).
- [13] R. Coisson, in "*Partical Accelerators*", **Volumn II**, p245, Gordon and Breach, NY (1981).
- [14] J.S. Wurtele et al. *Phys. Fluids*, **B2**, p401 (1990).
- [15] R. Prazeres and J. M. Ortega, *Nucl. Instrum. Meth. in Phys. Res.* **A296**, p436 (1990); also *Nucl. Instrum. Meth. in Phys. Res.* **A304**, p72 (1990).
- [16] I. Ben-Zvi et al., *Nucl. Instrum. Meth. in Phys. Res.* **A318**, p208 (1992).

- [17] N.Piovella et al., *Phys. Rev. Lett.* **72** p88 (1994).
- [18] E.Steinbach and H.Ghalila, *Nucl. Instrum. Meth. in Phys. Res.* **A304**, p691 (1991).
- [19] C.Wang, J.L. Hirshfield, and A.K. Ganguly, *Phys. Rev. Lett.* **77** p3819 (1996).
- [20] Example in A. Yariv, *Quantum Electronics* ed. by Wiley, New York, Ch.22.

Chapter 2

Theory and FEL Equations

In this chapter, we first review the basic FEL theories that describe the fundamental physics involved in the free electron laser. Then we introduce the "FEL resonant harmonic conversion" theory, including the deduction of the set of coupled FEL equations with slippage for the electron dynamics and two interacting waves. In the end, we introduce the "7th harmonic co-generation" concept, and its corresponding theoretical model.

2.1 The Basic FEL theory

Several books [1,2] and review articles [3,4,5] give excellent overviews of the fundamental physics involved in the free electron laser. Although the FEL theory was quantum mechanical initially [6], it turns out that a quantum description of FEL is unnecessary unless the photon energy is comparable with the electron rest energy. Colson [7] showed that the two-wave Compton FEL could be modeled as an electromagnetic problem with a pendulum equation. Sprangle and Tang [8] generalized the pendulum equation to include the space-charge effect for a Raman FEL.

2.1.1 The Basic FEL Equations

Based on Cai's derivation [9], we introduce the following FEL equations, which are a set of first order differential equations of electron motion in phase space together with a wave equation for the radiation which is obtained by using the electron beam as the driving current. We treat the electron motion in one dimension and the wave in two dimension.

In a FEL, the relativistic electron beam enters a constant period and helically polarized undulator, where the undulator vector potential can be expressed as:

$$\hat{A}_w = -\frac{mc^2}{e} a_w [\hat{x} \cos(k_w z) + \hat{y} \sin(k_w z)] \quad (2.1)$$

where $a_w = eB_1 / k_w mc^2$ is the normalized vector potential, $k_w = 2\pi / l_w$ is the wavenumber of the undulator, and B_1 is the transverse undulator field on axis. The helical undulator induces a helical transverse motion of the electron beam, which is in the same plane as the electric field of the circularly polarized radiation EM wave. The vector product $\mathbf{j}_\perp \cdot \mathbf{E}_\perp$ of the electron transverse velocity and this electric field acts on the electrons and allows an energy exchange between the electrons and the radiation.

The vector potential associated with the signal wave that is circularly polarized and propagates in the z direction in the undulator is of form:

$$\hat{A}_s = \frac{mc^2}{e} a_s [\hat{x} \cos(k_s z - \omega t + \phi) - \hat{y} \sin(k_s z - \omega t + \phi)] \quad (2.2)$$

where $a_s = eB_s / k_s mc^2$ is the normalized vector potential, $k_s = 2\pi / \lambda_s = \omega / c$ is the signal wave number in vacuum, ω is the wave frequency and ϕ is the phase shift of the wave. Generally, A_s is much smaller than A_w ($A_s \ll A_w$), but this signal magnetic field is important because its cross product with the electron transverse velocity gives rise to the sinusoidal axial ponderomotive force $(-\frac{e}{c} \hat{v}_\perp \times \hat{B}_s)$ that bunches the electron beam, enabling a net average energy exchange between the electron beam and the radiation field to occur.

We define a phase angle θ which describes the phase of the electron relative to the signal wave at position z and time t :

$$\theta = (k_w + k_s)z - \omega t \quad (2.3)$$

then

$$\frac{d\theta}{dz} = k_w + k_s - \frac{k_s c}{v_z} \quad (2.4)$$

An electron moving in the EM fields given by Eq.(2.1)-(2.2) has a conservative transverse canonical momentum, $\hat{P}_\perp = \gamma m \hat{v}_\perp - \frac{e}{c} \hat{A} = \text{constant}$, where $\hat{A} = \hat{A}_w + \hat{A}_s$ and $\gamma^2 = \left(1 - \frac{v_z^2}{c^2} - \frac{v_\perp^2}{c^2}\right)^{-1}$. From this equation, we can get:

$$\frac{v_z}{c} = \sqrt{1 - \frac{1}{\gamma^2} - \left(\frac{e}{mc^2}\right)^2 \frac{\hat{A}^2}{\gamma^2}} \approx \sqrt{1 - \frac{1 + a_w^2}{\gamma^2}} \quad (2.5)$$

. Thus the phase equation of the electron motion can be obtained from Eq.(2.4) and (2.5):

$$\frac{d\theta_j}{dz} = k_w \left(1 - \frac{\gamma_r^2}{\gamma_j^2}\right) \quad (2.6)$$

where $\gamma_r^2 = \frac{k_s(1 + a_w^2)}{2k_w}$ is the resonant electron energy, and the subscript "j" is the index of the j'th electron (Note $\frac{d\theta_j}{dz} = 0$, if $\gamma_j = \gamma_r$).

Another dynamic equation for a single electron is obtained from the energy conservation law, $\frac{d}{dt}(\gamma mc^2) = -e\hat{v} \cdot \hat{E}$; it can be shown that the electron energy equation has following form:

$$\frac{d\gamma_j}{dz} = -\frac{a_w a_s \omega}{\gamma_j v_z} \sin \psi_j + \frac{2\omega_p^2 v_z}{\omega c^2} [\langle \cos \psi \rangle \sin \psi_j + \langle \sin \psi \rangle \cos \psi_j] \quad (2.7)$$

where $\psi = \theta + \phi = (k_w + k_s)z - \omega t + \phi$, and the angular bracket indicates the ensemble average for all the electrons. The first term on the right hand side of the above equation comes from the ponderomotive force, and the second term comes from the electrostatic force from the plasma wave that is special to the Raman FEL.

The wave equation for the vector potential in the signal radiation driven by the electron current can be derived by solving the Maxwell equation. We define $a = a_s e^{i\theta}$ as the complex amplitude of the normalized signal vector potential. Using the slow varying variable assumption (eikonal approximation) for the signal complex amplitude, the wave equation can be written as:

$$(\nabla_{\perp}^2 + 2ik_s \frac{\partial}{\partial z} + 2i \frac{\omega}{c^2} \frac{\partial}{\partial t})a = -\frac{\omega_p^2 a_w}{c^2} \left\langle \frac{e^{-i\theta}}{\gamma} \right\rangle \quad (2.8)$$

If we treat the wave as one dimensional, the ∇_{\perp}^2 term can be dropped, then the wave equation can be rewritten as:

$$\left(\frac{\partial}{\partial z} + \frac{1}{c} \frac{\partial}{\partial t} \right) a = i \frac{\omega_p^2 a_w}{2c^2 k_s} \left\langle \frac{e^{-i\theta}}{\gamma} \right\rangle \quad (2.9)$$

We therefore have derived a complete set of FEL equations Eq.(2.6), (2.7) and (2.9).

2.2 The FEL Resonant Harmonic Conversion Theory

The equation set we derived in the previous section is for the Raman FEL in the free space, which means no waveguide is present. In our system, the electron beam travels along the axis of a cylindrical drift tube, which serves as a waveguide for the microwave radiation output. Also in a waveguide, there are two unstable root of the dispersion relation, which represent two growing waves. So we need a theory to describe the nonlinear interaction between the two waves in the waveguide FEL. For simplicity, we first deduce the Compton model by ignoring the space charge effect.

2.2.1 The Compton Waveguide FEL Equation with Slippage

Let us consider the radiation wave traveling in a waveguide, instead of the vacuum. The vector potential is in the following form $A_s = \frac{mc^2}{e} a_s e^{i(kz - \omega t)}$, where

$$\omega^2 = c^2(k^2 + k_\perp^2) \quad (2.10)$$

where k and k_\perp are the longitudinal and the transverse components of the wave vector. Eq.(2.10) is the dispersion relation for a wave traveling in an empty waveguide. From this dispersion relation, one can get the phase velocity v_p and group velocity v_g :

$$v_p = \omega/k = c/n \quad (2.11)$$

$$v_g = d\omega/dk = cn \quad (2.12)$$

where $v_p v_g = c^2$ and $n = \sqrt{1 - (k_\perp/k)^2}$, the waveguide index.

For the electron beam propagating in a wiggler with period l_w , the relative phase between the electron and the radiation wave is defined as $\theta = (k_w + k)z - \omega t$. Following the similar procedure as we used in section 2.1, we can obtain the modified phase equation [10]: $\frac{d\theta}{dz} = k_w + k - \sqrt{k_w^2 + k^2} c/v_z$, which can be written in the following standard form:

$$\frac{d\theta}{dz} = \bar{k}_w \left(1 - \frac{\gamma_r^2}{\gamma^2} \right) \quad (2.13)$$

where

$$\bar{k}_w = k_w + k - \omega/c \quad (2.14)$$

and

$$\gamma_r^2 = k(1 + a_w^2) / 2\bar{k}_w \quad (2.15)$$

Hence the waveguide modifies the resonance energy comparing to Eq.(2.6).

It is easy to see that the electron energy evolution equation remains unchanged with respect to the case without waveguide, but we drop the Raman effect term in Eq. (2. 7), since we are deducing the Compton model :

$$\frac{d\gamma_j}{dz} = -\frac{a_w a_s \omega}{\gamma_j v_z} \sin \psi_j \quad (2.16)$$

The field amplitude equation (Eq. 2.9) is modified by simply substituting [10, 11] the vacuum speed of light by the group velocity v_g (Eq. 2.12) and the wavenumber k_s by the longitudinal wavenumber k :

$$\left(\frac{\partial}{\partial z} + \frac{1}{v_g} \frac{\partial}{\partial t}\right) a = i \frac{\overline{\omega_p^2} a_w}{2c^2 k} \left\langle \frac{e^{-i\theta}}{\gamma} \right\rangle \quad (2.17)$$

where $\overline{\omega_p^2} = 4\pi e^2 \overline{n_e} / m$ is the modified plasma frequency, and $\overline{n_e}$ is the electron current density with respect to mode cross section. Again in this equation, a has no transverse dependence.

For the electron beam, since the phase θ and energy γ are both function of z and t , we should replace $\frac{d}{dz}$ by $\frac{\partial}{\partial z} + \frac{\partial}{\partial t} \frac{\partial t}{\partial z} = \frac{\partial}{\partial z} + \frac{1}{v_z} \frac{\partial}{\partial t}$, where $\frac{\partial z}{\partial t} = v_z$ is the electron axial velocity. The complete set of the waveguide Compton FEL equations for N electrons is:

$$\left(\frac{\partial}{\partial z} + \frac{1}{v_z} \frac{\partial}{\partial t}\right) \theta_j = \overline{k_w} \left(1 - \frac{\overline{\gamma_r^2}}{\gamma_j^2}\right) \quad j = 1, \dots, N; \quad (2.18)$$

$$\left(\frac{\partial}{\partial z} + \frac{1}{v_z} \frac{\partial}{\partial t}\right) \gamma_j = -\frac{a_w a_s \omega}{\gamma_j v_z} \sin \psi_j \quad j = 1, \dots, N; \quad (2.19)$$

$$\left(\frac{\partial}{\partial z} + \frac{1}{v_g} \frac{\partial}{\partial t}\right) a = i \frac{\overline{\omega_p^2} a_w}{2c^2 k} \left\langle \frac{e^{-i\theta}}{\gamma} \right\rangle \quad (2.20)$$

with $\langle F \rangle_{z,t} = \frac{1}{N} \sum_{j=1}^{N(z,t)} F_j$.

2.2.2 The Two Resonant Waves in the Waveguide FEL

The dispersion relation for an empty waveguide is given by Eq. (2.10): $\omega^2 = c^2(k^2 + k_\perp^2)$, where $k_\perp = 2\pi/l_c$ and l_c is the cut-off wavelength. In particular, for the TE_{11} mode in a cylindrical waveguide with inner radius R_s , $l_c = 2\pi R_s / 1.84$. For the Compton FEL, the resonance condition on the axial velocity $v_\parallel = c\beta$ of the electron beam requires that the electron travels a wiggler period l_w in the same time that the wave travels a distance $l_w + \lambda$ ($\lambda = 2\pi/k$) at the phase velocity ω/k , so that

$$\omega = c\beta(k + k_w) \quad (2.21)$$

By equating Eq.(2.10) and (2.19), one obtains, for $k_\perp \leq \beta\gamma_1 k_w$ (where $\gamma_1 = (1 - \beta^2)^{-1/2}$), the expression of the two resonant frequencies neglecting the beam space charge effects [12]:

$$\omega_{1,2} = \frac{\omega_s}{1 + \beta} [1 \pm \beta\sqrt{1 - X}] \quad (2.22)$$

where

$$\omega_s = \frac{c\beta k_w}{1 - \beta} \quad (2.23)$$

is the free-space resonant frequency and $X = \left(\frac{l_w}{\beta\gamma_1 l_c} \right)^2$ is the waveguide parameter [10]

$0 \leq X \leq 1$. As shown in Fig. 2.1, the ω_1 and ω_2 are the two upper and lower intersection between the "beam line" and the "waveguide line". The two roots merge at the "tangency" condition $X = 1$.

We also introduce the frequency ratio parameter [11]

$$\alpha = \frac{\omega_1}{\omega_2} = \frac{1 + \beta\sqrt{1 - X}}{1 - \beta\sqrt{1 - X}} \quad (2.24)$$

with $1 \leq \alpha \leq \frac{1 + \beta}{1 - \beta}$. When α is a integer, then ω_1 is the harmonic wave of ω_2 .

Furthermore, the group velocities relative to the resonant frequencies are $v_{g1,2} = c^2(k_{1,2}/\omega_{1,2})$.

By definition (Eq. 2.14), $\bar{k}_w = k_w + k - \omega/c$, and also $\omega = c\beta(k + k_w)$ (Eq. 2.21), $\omega_s = \frac{c\beta k_w}{1-\beta}$ (Eq. 2.23), it is easy to prove that

$$\bar{k}_w = k_w \omega / \omega_s \quad (2.25)$$

If we define

$$\theta_{1,2} = (k_w + k_{1,2})z - \omega_{1,2}t \quad (2.26)$$

as the relative phase between the electron and the two separate waves, then we can get

$$\theta_1 / \theta_2 \approx \bar{k}_{w1} / \bar{k}_{w2} \quad (2.27)$$

with $z/t = v_1 \approx c$. Based on both Eq.(2.27) and (2.25), we can obtain

$$\theta_1 / \theta_2 \approx \alpha \quad (2.28)$$

which is a relation used for deriving the following two resonant wave model.

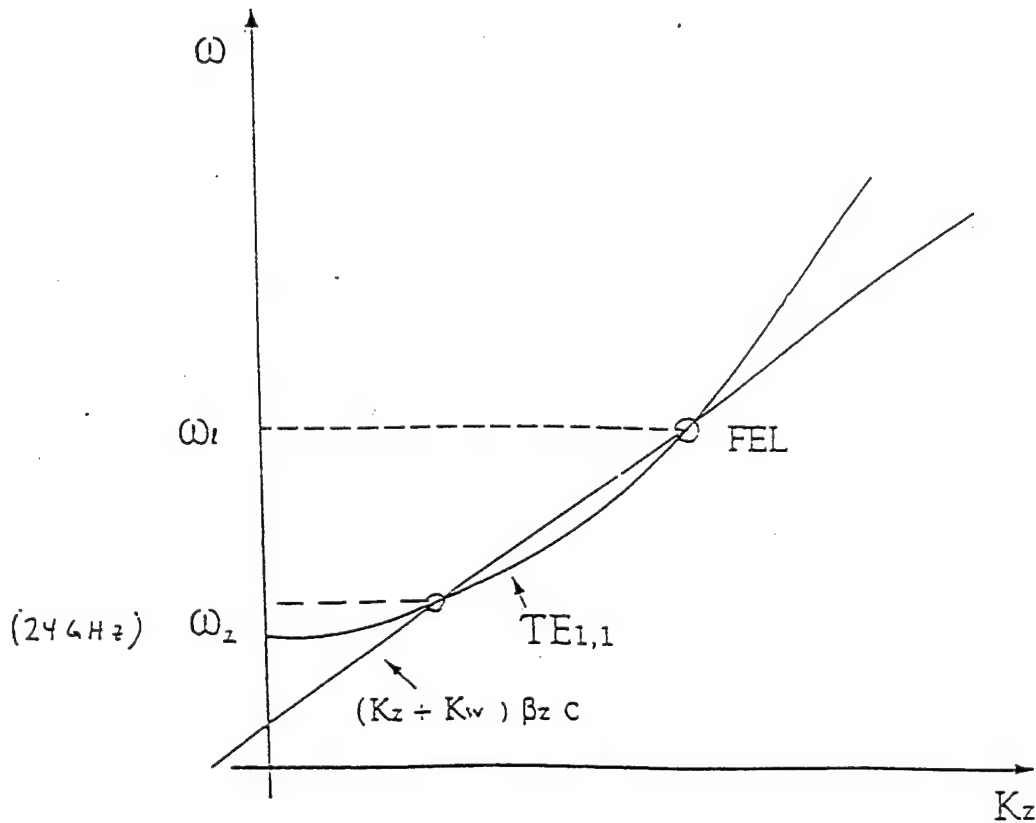


Figure 2.1 The two roots of the waveguide FEL at the intersections.

2.2.3 The Two Resonant Wave Compton Model

The existence of two resonant frequencies requires us to develop a theory to describe the coupling between the two waves as a result of the nonlinear interaction. We derive the following equations by ignoring the interference effects between the two waves.

First we consider the electron phase equation. Since the two relative phases θ_1 and θ_2 are correlated with each other (Eq.2.28) for the two resonant waves ω_1 and ω_2 , we can just keep one phase equation, (say θ_2) to describe the resonant relationship. By substituting θ by θ_2 and \bar{k}_w by \bar{k}_{w2} , we can get the following phase equation:

$$\left(\frac{\partial}{\partial z} + \frac{1}{v_i} \frac{\partial}{\partial t} \right) \theta_{2j} = \bar{k}_{w2} \left(1 - \frac{\gamma_{r2}^2}{\gamma_j^2} \right) \quad (2.29)$$

with $\gamma_{r2}^2 = k_2(1 + a_w^2) / 2\bar{k}_{w2}$, the common resonant energy for both ω_1 and ω_2 to be resonant with the electron.

Next we derive the electron energy equation, where the coupling term between the two waves occurs. The electric field of the TE_{11} mode in the waveguide is the sum of the two resonant frequency components:

$$A_s = A_{s1} + A_{s2} \quad (2.30)$$

with $A_{s1} = \frac{mc^2}{e} a_{s1} e^{i(k_1 z - \omega_1 t)}$ and $A_{s2} = \frac{mc^2}{e} a_{s2} e^{i(k_2 z - \omega_2 t)}$, and then there should be two terms instead of one (Eq.2.19) on the right hand side of the energy equation:

$$\left(\frac{\partial}{\partial z} + \frac{1}{v_i} \frac{\partial}{\partial t} \right) \gamma_j = - \frac{a_w}{\gamma_j v_w} (a_{s1} \omega_1 \sin \psi_{1j} + a_{s2} \omega_2 \sin \psi_{2j}) \quad (2.31)$$

with $\psi_1 = \theta_1 + \phi_1 = \alpha \theta_2 + \phi_1$ and $\psi_2 = \theta_2 + \phi_2$.

There should be two wave equations to describe the evolution of the two wave amplitude a_1 and a_2 ($a_{1,2} = a_{s1,2} e^{-i\phi_{1,2}}$):

$$\left(\frac{\partial}{\partial z} + \frac{1}{v_{g1}} \frac{\partial}{\partial t}\right) a_1 = i \frac{\overline{\omega_p^2} a_w}{2c^2 k_1} \left\langle \frac{e^{-ia\theta_1}}{\gamma} \right\rangle \quad (2.32)$$

$$\left(\frac{\partial}{\partial z} + \frac{1}{v_{g2}} \frac{\partial}{\partial t}\right) a_2 = i \frac{\overline{\omega_p^2} a_w}{2c^2 k_2} \left\langle \frac{e^{-i\theta_2}}{\gamma} \right\rangle \quad (2.33)$$

with the bunching current on the right hand of the equations.

We have derived the complete set of first-order differential equations (Eq.(2.29), (2.31), (2.32) and (2.33)) to describe the space and time interaction of the two resonant waves in a waveguide FEL. These equations will predict excessive growth for the waves, because in the 1D theory, there is perfect overlap between the wave amplitude and the electrons. To model this, it is necessary to introduce a "filling factor" into the right hand side of the radiation wave equations (Eq. 2.32, 2.33). The filling factor is approximately the ratio of the electron beam area to the waveguide area. In the application of this, we have in mind that ω_2 is the powerful FEL-resonant lower frequency wave driven by a laboratory source, and ω_1 is a lower power harmonic wave, which is also FEL resonant mode and its growth will be enhanced by the harmonics of bunching induced by ω_2 .

2.3 The 7th Harmonic Co-generation Theory

As we mentioned in Chapter 1, coherent radiation can be generated at the 7th harmonic by a "co-generation" mechanism, since it is found that the lowest TE_{s1} mode in a cylindrical waveguide at frequency $s\omega$ that has group velocity nearly matching with the TE_{11} mode at frequency ω is the $TE_{7,2}$ mode.

2.3.1 Co-generation Group Velocity Matching

For the "co-generation" mechanism, the requirement for group velocity matching for efficient power transfer between two guided waves that interact with an electron beam

can be easily derived. Below are the resonance conditions that must be satisfied for a TE_{11} Compton FEL (see Eq.(2.21)) and the s -th TE_{sl} harmonic radiation generation:

$$\omega = c\beta k_{z,11} + c\beta k_w \quad (2.34)$$

and

$$s\omega = c\beta k_{z,sl} + c\beta sk_w \quad (2.35)$$

where $k_{z,sl} = \omega n_{sl}/c$ is the axial wavenumber, and

$$n_{sl} = \sqrt{1 - \left(\lambda/l_{c,sl}\right)^2} \quad (2.36)$$

is the waveguide index or normalized group velocity [13] for each wave, where $l_{c,sl}$ is the cut-off wavelength of each wave.

Clearly, Eq.(2.34) and (2.35) cannot be satisfied simultaneously unless

$$\frac{k_{z,sl}}{s} = k_{z,11} \quad \text{or} \quad n_{sl} = n_{11} \quad (2.37)$$

namely equal group velocities for the two modes, when the frequency of the TE_{sl} mode is s times that of the TE_{11} mode. This is consistent with the selection rule for harmonic conversion with an axis-encircling beam in a cylindrical waveguide, namely that power at the s -th harmonic can flow cumulatively from the beam only into TE_{sl} modes [14].

For the TE_{sl} modes in a cylindrical waveguide, n_{sl} can be written as:

$$n_{sl} = \sqrt{1 - \left(j'_{sl}c/s\omega R\right)^2} \quad (2.38)$$

where j'_{sl} is the l -th zero of the Bessel function derivative $(d/dx)J_s(x)$, and R is the waveguide radius. When $n_{sl} \approx n_{11}$, one can derive the approximate relationship:

$$\frac{n_{sl}}{n_{11}} \approx 1 + (1 - r_{sl}) \left(\frac{1}{n_{11}^2} - 1 \right) \quad (2.40)$$

where $r_{sl} = \frac{j_{sl}'}{sj_{11}'}$ is the normalized root.

Fig. 2.2 are plotted values of r_{sl} for modes with l (the radial index) up to 6, and s (the azimuthal index) up to 30. it is seen that r_{sl} is within the range 1.00 ± 0.005 for the $TE_{7,2}$, $TE_{13,3}$, $TE_{24,5}$ and $TE_{30,6}$ modes. Among all those modes, $TE_{7,2}$ is the lowest mode for which a near match in group velocity obtains, which suggests the 7th harmonic co-generation. In the application of this concept, we need to move the electron beam off-axis, to overlap one of the electric field maxima of the $TE_{7,2}$ wave, since the $TE_{7,2}$ has zero transverse E fields on axis.

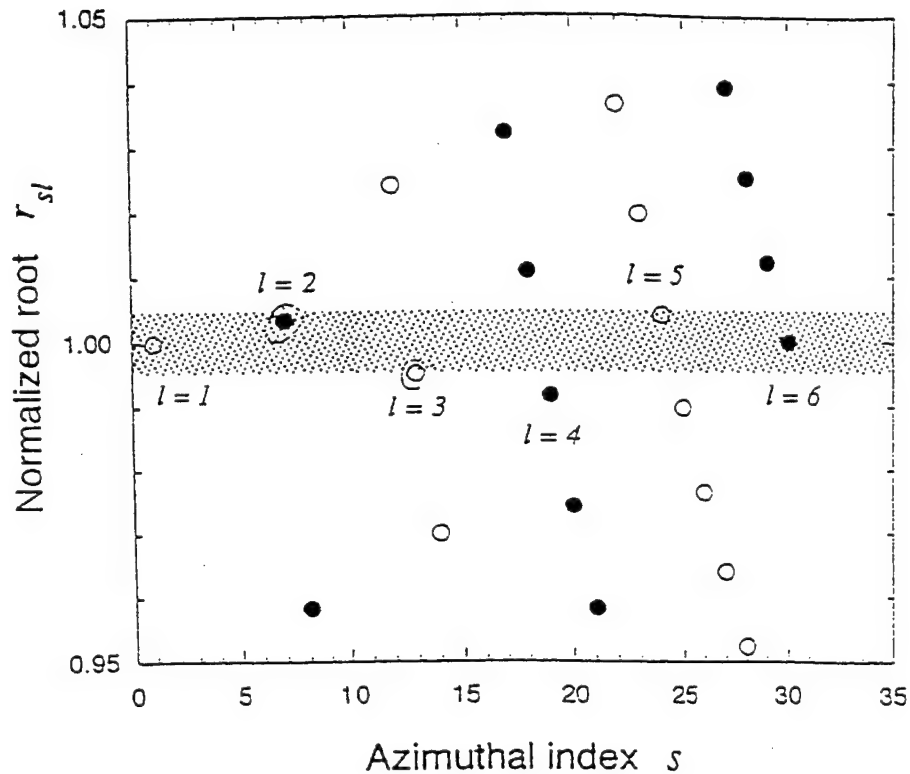


Figure 2.2 Ratio of Bessel function roots r_{sl} . In shaded area $0.995 < r_{sl} < 1.005$. [12]

2.3.2 The 2-wave Model for the 7th Harmonic Co-generation

For the 7th harmonic co-generation, we also have two waves ω_1 and ω_2 , with $\omega_1 = 7\omega_2$, the $TE_{7,2}$ 7th harmonic of the fundamental $TE_{1,1}$ ω_2 . In order to study the interaction between these two waves, we also need to develop a set of equations to describe the time and space evolution of these two waves.

First we define the relative phase between the electron and the 7th harmonic ω_1 :

$$\theta_1 = (7k_w + k_1)z - \omega_1 t \quad (2.41)$$

where k_w is the wiggler wavenumber and k_1 is the 7th harmonic axial wavenumber. The definition of the relative phase between the electron and the fundamental wave ω_2 is still given by Eq.(2.26): $\theta_2 = (k_w + k_2)z - \omega_2 t$. Since the group velocity between the 7th harmonic ω_1 and wave ω_2 are nearly matched, we can get the following relation from Eq.(2.37):

$$k_1 \approx 7k_2 \quad (2.42)$$

And we know that $\omega_1 = 7\omega_2$, based on those two relations and the definitions for θ_1 and θ_2 , it is very obvious to obtain that:

$$\theta_1 \approx 7\theta_2 \quad (2.43)$$

which is consistent with Eq.(2.28). So we can adapt the 2-wave Compton model introduced in section 2.2.3 to describe the 7th harmonic co-generation.

Following the similar processes given in section 2.2.3, we get the following first-order partial differential equations:

$$\left(\frac{\partial}{\partial z} + \frac{1}{v_1} \frac{\partial}{\partial t} \right) \theta_{2j} = \bar{k}_{w2} \left(1 - \frac{\gamma_{r2}^2}{\gamma_j^2} \right) \quad (2.44)$$

where $\gamma_{r2}^2 = k_2(1 + a_w^2) / 2\bar{k}_{w2}$ and $\bar{k}_{w2} = k_w + k_2 - \omega_2/c$. This is the electron phase equation that describes the resonant condition.

$$\left(\frac{\partial}{\partial z} + \frac{1}{v_1} \frac{\partial}{\partial t}\right) \gamma_j = -\frac{a_w}{\gamma_j v_{uj}} (a_{s1} \omega_1 \sin \psi_{1j} + a_{s2} \omega_2 \sin \psi_{2j}) \quad (2.45)$$

where $\psi_1 = 7\theta_2 + \phi_1$ and $\psi_2 = \theta_2 + \phi_2$. This is the electron energy equation which describes the energy transfer between the two waves and the electron beam.

$$\left(\frac{\partial}{\partial z} + \frac{1}{v_{g1}} \frac{\partial}{\partial t}\right) a_1 = i \frac{\overline{\omega_p^2} a_w}{2c^2 k_1} \left\langle \frac{e^{-i7\theta_2}}{\gamma} \right\rangle \quad (2.46)$$

and

$$\left(\frac{\partial}{\partial z} + \frac{1}{v_{g2}} \frac{\partial}{\partial t}\right) a_2 = i \frac{\overline{\omega_p^2} a_w}{2c^2 k_2} \left\langle \frac{e^{-i\theta_2}}{\gamma} \right\rangle \quad (2.47)$$

are the two waves equations that describe the evolution of the two waves under the driving the electron bunching current.

This one-dimensional model cannot take account of the different filling factors caused by the overlap of ω_2 in TE_{11} mode and ω_1 in $TE_{7,2}$ mode, nor can it model the off-axis beam displacement. A 3D model is really needed for this physics [14].

2.4 The Two -wave Raman Model

Since our FEL is working in a Raman regime, it is necessary to have a Raman version of the theory. As we mentioned in Chapter one, the space-charge effect downshifts the effective wiggler period in the following way:

$$k_{w(Compton)} = k_{w(Raman)} - \frac{\omega_p}{\gamma v_{\parallel}} \quad (2.48)$$

so, we should substitute the k_w by $k_w - \frac{\omega_p}{\gamma v_{\parallel}}$ whenever k_w appears. Then the formula (Eq.2.22) giving the two resonant frequencies should stay the same by doing the above

substitution. In order to give the same two resonant modes, we need shorter wiggler period which can be calculated from Eq.(2.48).

But for the 2-wave model FEL equations, except the substitution, there should be extra Raman terms on the right hand side of the electron energy equation:

$$\begin{aligned} \left(\frac{\partial}{\partial z} + \frac{1}{v_i} \frac{\partial}{\partial t} \right) \gamma_j = & -\frac{a_w}{\gamma_j v_{ij}} (a_{s1} \omega_1 \sin \psi_{1j} + a_{s2} \omega_2 \sin \psi_{2j}) \\ & + \frac{2\omega_p^2}{k_1 c^2} [\langle \cos \psi_1 \rangle \sin \psi_{1j} - \langle \sin \psi_1 \rangle \cos \psi_{1j}] + \frac{2\omega_p^2}{k_2 c^2} [\langle \cos \psi_2 \rangle \sin \psi_{2j} - \langle \sin \psi_2 \rangle \cos \psi_{2j}] \end{aligned} \quad (2.49)$$

all other three equations will stay the same form excepting doing substitution when it is necessary. The Raman terms result from the axial electric space charge fields of the bunched beam, and it will weaken the FEL interaction.

References:

- [1] T.C.Marshall, Free-Electron Lasers (Macmillan Publishing Co., New York, 1985)
- [2] The Free Electron Laser Handbook, ed. W.B. Colson, C. Pellegrini, and A. Renieri (Elsevire Science Publishing Co., New York, 1989).
- [3] R. Bonifacio et al, *Optics Communication* **61** p55 (1987).
- [4] R.Bonifacio, B. W. J. McNeil, and P. Pierini, *Phys. Rev. A*, **40**, p4467 (1989).
- [5] N.M. Kroll, P.L. Morton, and M.N. Rosenbluth, *IEEE J. Quant. Elect.* **QE-17**, p1436 (1981).
- [6] J.M.Madey, *J. Appl. Phys.* **42**, p1906 (1971).
- [7] W.B. Colson, *Phys. Quan. Elec.* **5**, p152 (1977).
- [8] P. Sprangle and C.M. Tang, *Tran. Nucl. Sci.* **NS-28**, p3346 (1981). .
- [9] S.Y.Cai, Doctoral Thesis, Columbia Univ. (1989).
- [10] R. Bonifacio and L. De Salvo Souza, *Nucl. Instr. and Meth.* **A289**, p394 (1989).
- [11] S.S. Yu et al, 9th FEL Conf., Williamsburg (1987).
- [12] N.Piovella et al., *Phys. Rev. Lett.* **72** p88 (1994).
- [13] C.Wang, J.L. Hirshfield, and A.K. Ganguly, *Phys. Rev. Lett.* **77** p3819 (1996).
- [14] J. Hirshfield et al, *Phys. Rev. E*, **47** p4364 (1993).
- [15] H.P. Freund and A.K. Ganguly, *Phys. Rev. A*, **34**, p1242 (1986).

Chapter 3

Experimental Apparatus

The experimental apparatus is discussed in three sections in this chapter: (1) the electron beam generation, (2) the FEL interaction, (3) the FEL diagnostics. Fig. 3.1 shows the physical layout of the FEL experimental equipment. In brief, a Marx bank and pulse forming line combination provides high voltage to the cathode of the vacuum diode. The electron beam is generated by the high-field emission from the graphite cathode and accelerated across the diode. A bifilar undulator supplies a circularly polarized, transverse magnetic field for the FEL interaction. The strong solenoidal magnetic field guides the electron beam and enhances the transverse motion stimulated by the undulator. The output radiation is spectrally diagnosed by a millimeter-wave "quasi-optical" spectrometer [1]. Oscilloscopes and detectors are used to study the radiation time structure and power level. A 24GHz magnetron provides a 10kW coherent signal to the input of the FEL, which amplifies this power about 40 times.

3.1 Electron Beam Generation

The relativistic electron beam in Columbia FEL is generated by a high voltage pulse line generator, Pulserad 220G manufactured by Physics International, Inc. The generator includes three major elements:

(1) the Marx capacitor bank, (2) the pulse forming line, and (3) the vacuum diode.

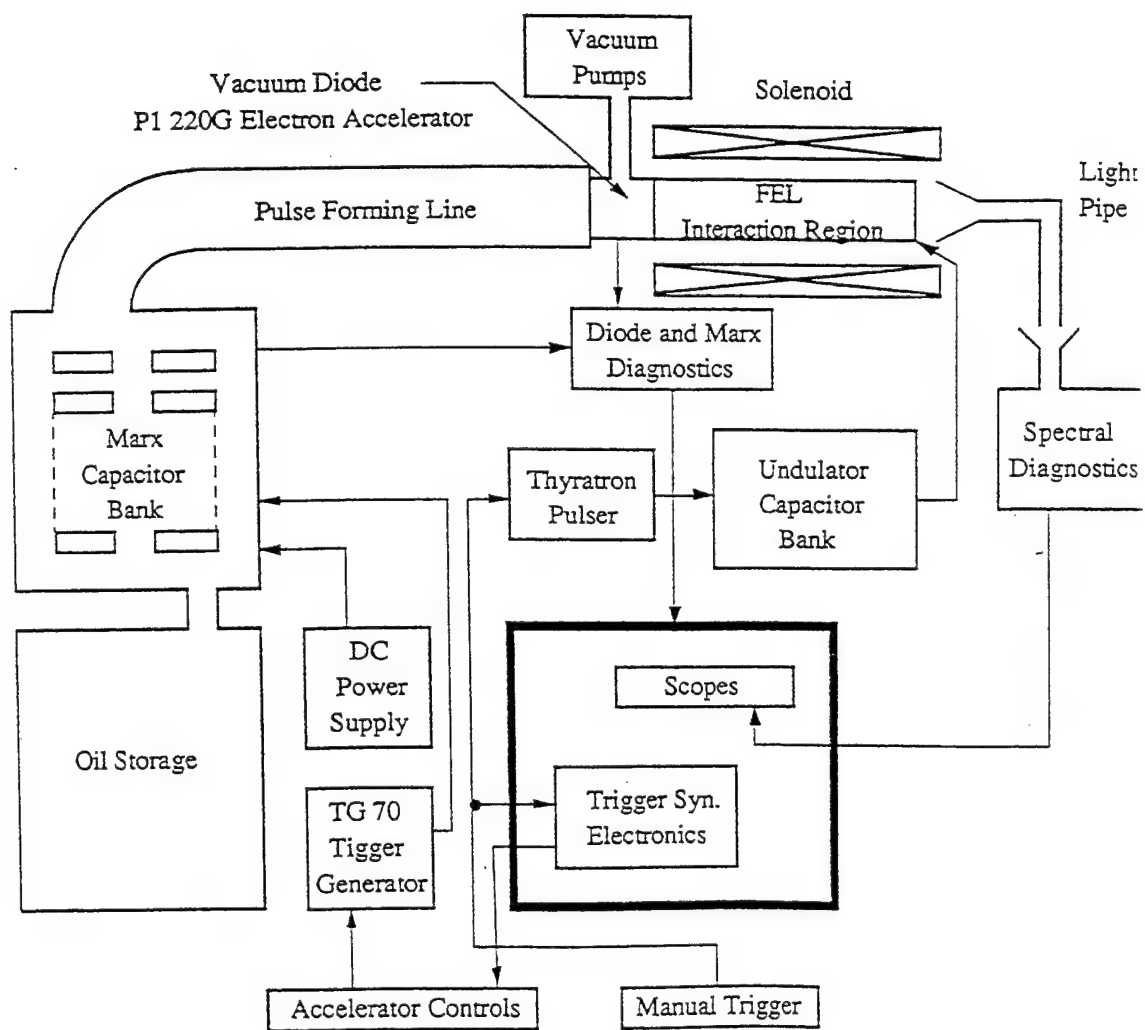


Figure 3.1 Schematic layout of the Raman FEL experimental apparatus.

3.1.1 Marx Capacitor Bank

Fig. 3.2 is the schematic of the Marx capacitor bank. A set of twenty high voltage capacitors is connected and charged in parallel through a series of interleaved water resistors. The capacitors are also connected in series by nineteen, midplane-triggered spark gaps. Another spark gap connects one end of the series connected capacitor train to ground. Another end of the capacitor train is connected by a final spark gap to a choke coil, which leads to the center conductor of the pulse forming line. All the capacitors are immersed in a tank of insulating oil, which can help to prevent arcing in the air at high voltage. The spark gaps are pressured with SF₆ gas, the gas pressure determines the breakdown voltage of the spark gap and is adjusted externally.

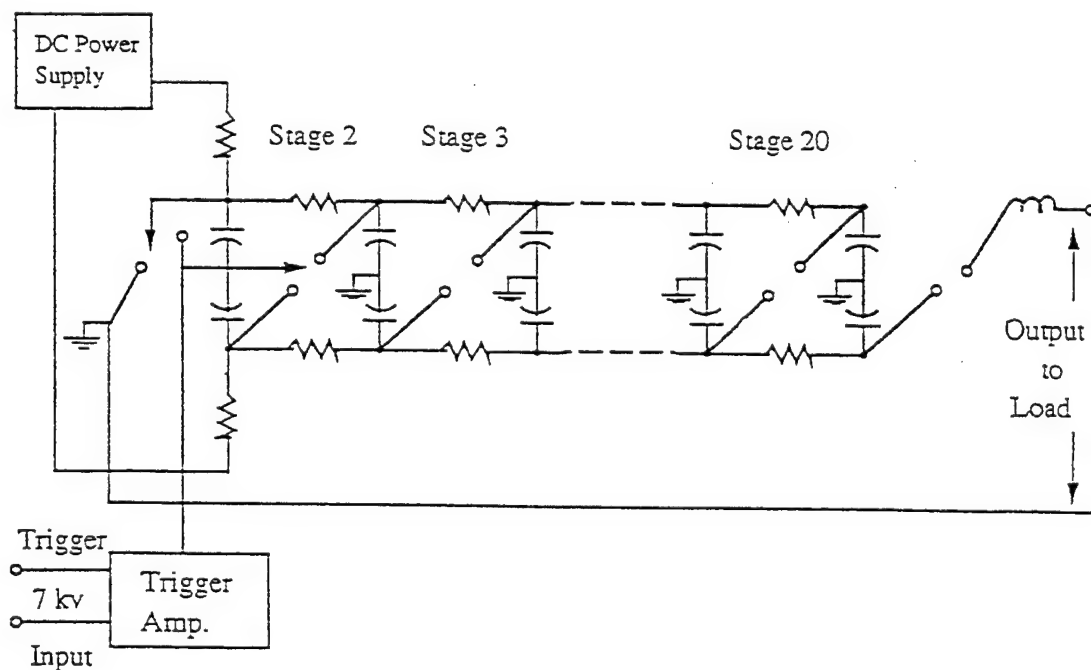


Figure 3.2 Schematic of the Marx capacitor bank.

Operation of the Marx bank is based on the same design patented by Professor Ersin Marx in 1923. After fully charging each capacitor to a desired voltage of 35kV, a 70kV trigger pulse is sent to the midplane of every other spark gap by the Marx trigger. The activated spark gaps double the voltage on every other capacitor which results in the overvoltage of the remaining spark gaps and the series discharge of the twenty capacitors. This forms a high voltage of $1.4\text{MV} = 2 \times 20 \times 35\text{kV}$ at the input of the transmission line. The Marx bank voltage is monitored by an electrode located at the output feed of the Marx bank to the transmission line which is shown in Fig. 3.3. A voltage divider and a series of attenuators are used to reduce the voltage to make sure it can be monitored on the oscilloscope.

3.1.2 Pulse Forming Line

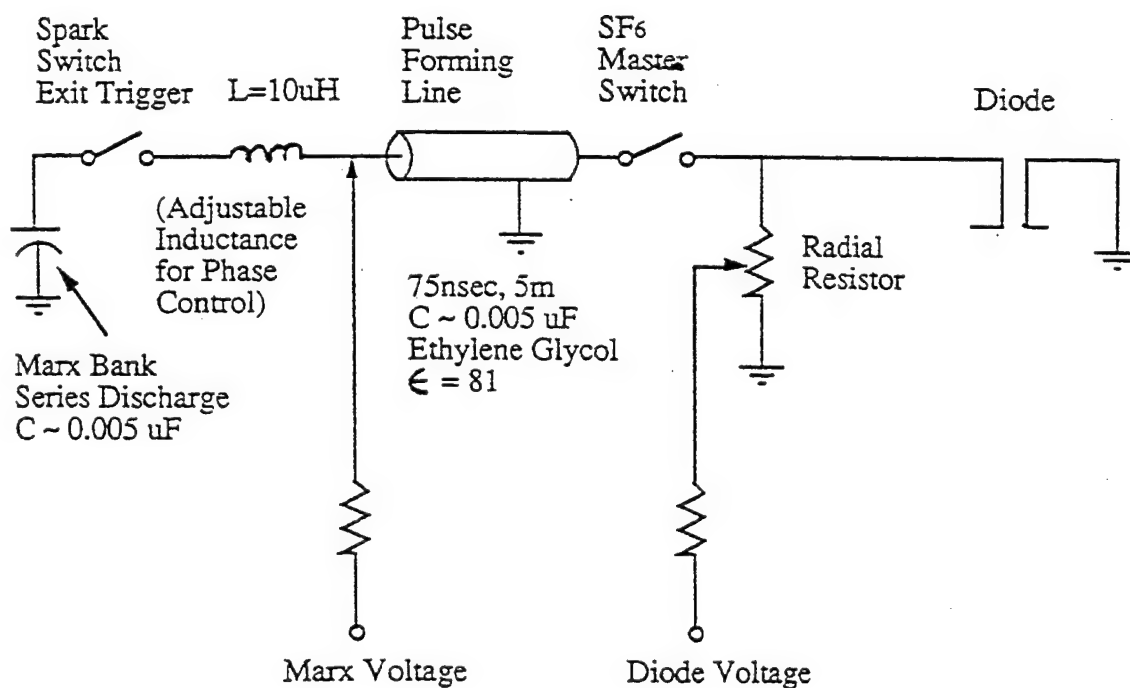


Figure 3.3 Circuit diagram of the pulse forming transmission line with associated accelerator elements.

Fig 3.3 depicts the schematic of the pulse beam generation system, which includes the Marx bank mentioned before, the pulse forming transmission line, the large high-field-emission triggered spark gap output switch, the impedance matching water resistor, and the vacuum diode.

The output voltage of the Marx bank following the choke coil behaves like a normal LC-circuit discharge:

$$V_{Marx} = V_0 \left[\cos\left(\frac{t}{\sqrt{LC}}\right) - 1 \right] \quad (3.1)$$

This voltage output is not suitable for generating the electron beam for the FEL where a constant beam energy is required. The pulse forming line conditions the output pulse from the Marx bank to a constant voltage pulse 150nsec long and passes it to the diode. The pulse forming line is a coaxial transmission line of 3.7meters long, with a tapered center conductor of average diameter 10cm, and an constant outer conductor of inner diameter 60cm. The space between the two conductors is filled with ethylene glycol. The output current from the Marx resonantly charges the center conductor of the transmission line. The voltage envelope on the center conductor follows Eq. 3.1, but the actual voltage is stair-stepped, each step lasting 150nsec, which is the round-trip transit time of an electromagnetic pulse traveling down the coaxial transmission line. When the voltage on the center conductor reaches a desired value, the gas Master switch abruptly closes and a constant voltage pulse of 150nsec is delivered to the diode through a close circuit with a matching impedance, which is provided by the radial water resistor. This way, the transmission line takes a sinusiodally varying voltage pulse and transfers it into a constant voltage pulse over 150nsec which is suitable for the FEL use.

The Master switch is a large spark gap, consisting a pair of metal electrodes with 4cm seperation, filled with SF₆ gas. Like the spark gaps in Marx bank, the break down voltage of the switch is determined by the gas pressure, which is regulated externally and is

independent of those in Marx bank. The gas pressure in this switch is the only way to fine tune the high voltage applied to the cathode of the vacuum diode. Unlike the midplaned triggered spark gap in Marx bank, the Master switch operates via high-field emission across the metal electrode. When the voltage on the charging electrode reaches the desired high break down voltage determined by the SF₆ pressure, high field emission occurs and the switch "closes" automatically.

The impedance matching water resistor is a coaxial container of about 8cm long, separating the Master switch from the vacuum diode. It is filled with 20 liters of distilled water doped with sodium thiosulphate (Na₂S₂O₃); the concentration of the solution determines the overall resistance. A water resistor with a conductivity of 180 μ mhos roughly matches the 23 Ω impedance on the end of the pulse forming line. The water resistor load dissipates about half of the pulse power, the remaining half propagates to the cathode, so the actual voltage appearing on the cathode is only half the Marx voltage, which in our case, is chosen to be about 600kV. The Diode voltage is monitored by a calibrated voltage divider and attenuator string of resistors.

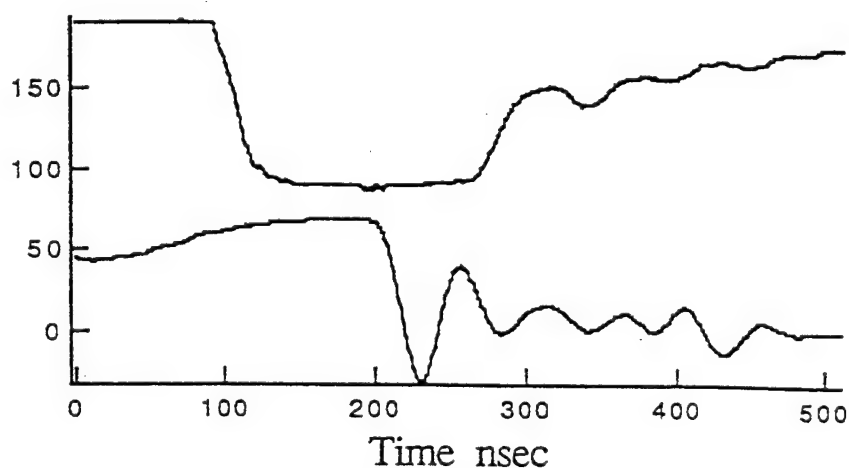


Figure 3.4 Oscilloscope traces of the diode voltage (upper trace) and the Marx bank voltage (lower trace).

Figure 3.4 is the typical oscilloscope trace of the diode voltage and the Marx bank voltage. The trace shows that the output Marx voltage grows sinusoidally as the transmission line is charged and then falls sharply as the output switch is closed. As for the diode voltage, it rises sharply at the beginning of the trace, then maintains a relatively constant voltage value for 150nsec, and falls down. The deviation of the voltage from a constant value during the pulse duration should not exceed 2-3%, however in practice, it is not easy to produce the flat pulse repeatedly.

3.1.3 Vacuum Diode

Figure 3.5 shows the geometry of the diode, the calculated equipotential surfaces and the electron trajectories in the vacuum diode region[2]. The diode is immersed in a strong 1 Tesla magnetic field of the soleniod, which helps to reduce the electron beam transverse velocity spread due to its own space charge.

The cathode is made of reactor grade graphite attached to the end of an aluminum cathode shank which is 30.5cm long and 7.62cm round. The graphite cathode is tapered to 2.5cm in diameter and rounded in the tip, shaped like an oblate hemisphere designed to produce parallel electron trajectories on the axis of the diode. On the microscopic scale, the surface of the graphite is rough. Small radius and microprotrusions enhance the local electric field greatly, causing the high field emission of electrons. A few nanoseconds after the ignition of the high field emission, the protrusions explode, producing a uniform electron emitting plasma over the whole surface of the cathode.

The anode is made of reactor grade graphite too. It is conically tapered with a 3mm diameter hole in the center to allow the electrons to pass through it and enter the FEL interaction region. Electrons emitted from the high potential cathode fall to the ground potential anode. Most of the electrons are intercepted (several kA). Only those on axis with minimal transverse velocity spread will continue to pass through the aperture (about 100A), follow the soleniodal magnetic field lines into the interaction region. Thus a low emittance

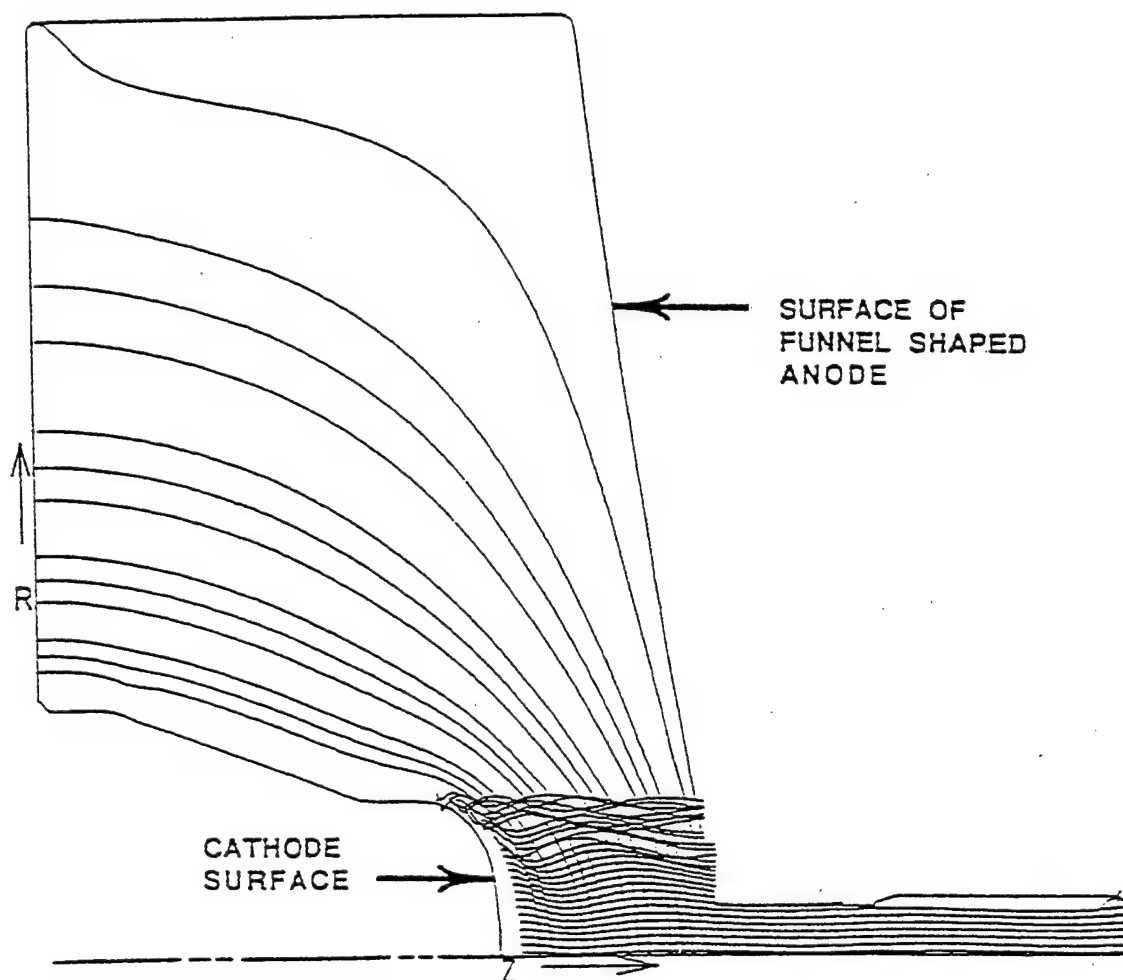


Figure 3.5 Calculated electron trajectories and equipotential surfaces in the vacuum diode.

electron beam is generated for the FEL, with an energy spread (without undulator) of

$$\frac{\Delta\gamma_1}{\gamma_1} = 0.6\% [3].$$

The diode voltage is monitored by a pair of electrodes located near the rim of the water resistor. The signal is attenuated for input to the measuring oscilloscope. The attenuation factor is about 10^5 in our project.

3.2 FEL Interaction

The interaction region contains the primary elements of the FEL: (1) the solenoid, (2) the FEL assembly, (3) the undulator. Fig. 3.6 diagrams the features of the equipments. Inside the FEL resonator, the relativistic electron beam interacts with circularly polarized, transverse magnetostatic field provided by the bifilar undulator, undergoes a spiralling motions and radiates coherently. The solenoid supplies a strong axial magnetic field to guide the electrons and enhance the transverse motion of the electrons.

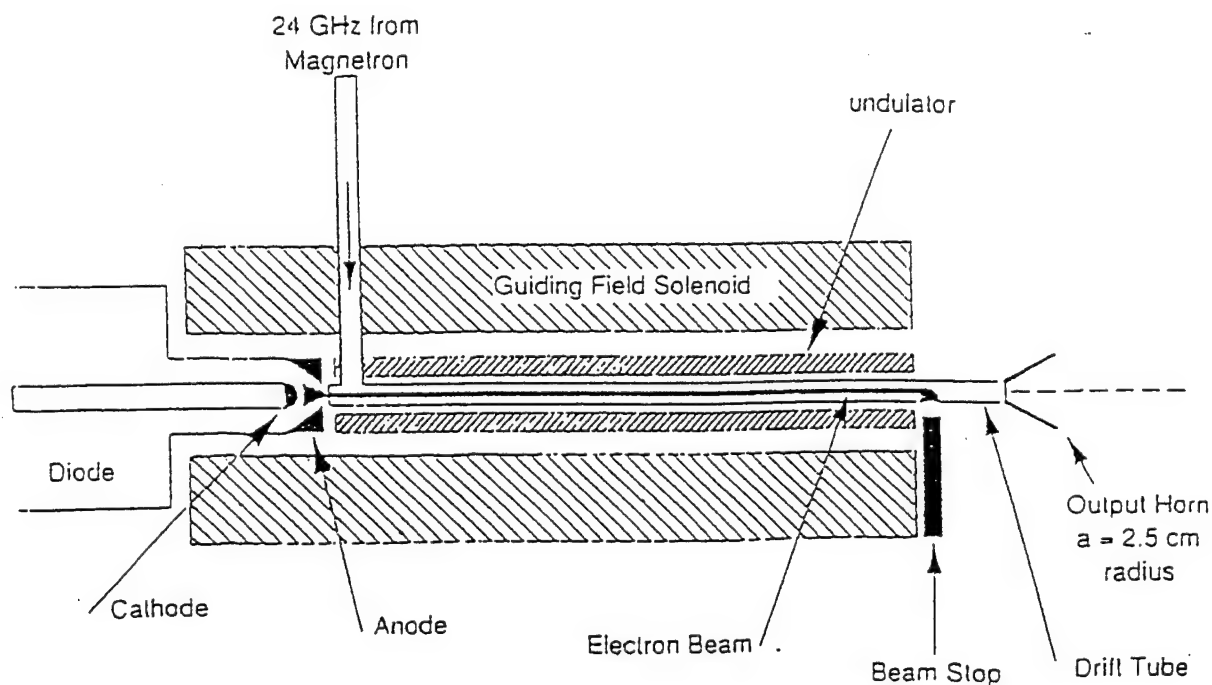


Figure 3.6 Schematic layout of the FEL interaction experimental apparatus..

3.2.1 The Solenoid

The solenoid supplies a strong (about 1 Tesla) constant axial magnetic field to confine the electron beam from transverse spreading due to the space charge effect. It is composed of 37 stacked copper coils connected in series, with a total length of 104cm. Each coil is a single tape-wound solenoid with integral water channel for cooling. The magnetic field depends linearly on the peak current applied to each coil. In the case of this project, a peak current of 1500 Amps is supplied to the coil and results in a net 0.9 Tesla magnetic field. The rectifiers in the power supply for the solenoid can withstand full current for only a few seconds before overheating. The current through the solenoid is manually raised and lowered quickly for each operation.

As mentioned before, the axial guiding field acts to confine the electron beam from spreading due to its own space charge field and to enhance the transverse motion of the electrons [4]. The enhancement is a result of the cyclotron motion of the electrons, induced by the guiding field, whereas helical motion is induced by the undulator. Without the guiding field, the helical quiver motion of the electrons is:

$$\frac{a_w}{\gamma} = \frac{v_{\perp}}{v_{\parallel}} \approx \frac{\Omega_{\perp}}{\gamma k_w \beta c}$$

where $a_w = eB_w l_w / 2\pi mc^2$, is the normalized undulator vector potential, and $\Omega_{\perp} = eB_w / mc$, B_w is the undulator magnetic field. Considering the cyclotron motion, the combined effective a_w is changed to :

$$\frac{a_w}{\gamma} = \frac{v_{\perp}}{v_{\parallel}} \approx \frac{\Omega_{\perp}}{\Omega_0 - \gamma k_w \beta c}$$

where $\Omega_0 = eB_0 / mc$, B_0 is the guiding magnetic field. Thus the effective "wiggler parameter" a_w increases as a result of this "cyclotron" term in the denominator. The quiver velocity of the electron (v_{\perp}) becomes large near the "magnetoresonance", $\Omega_0 = \gamma k_w \beta c$, may cause electrons to hit the walls of the drift tube and terminates the interaction. Thus

care should be taken to avoid this. In this case of project, the actual guiding field value is far from satisfying the magnetoresonance condition ($\Omega_0/2\pi \approx 25\text{GHz}$, $\gamma\kappa\beta c/2\pi \approx 30\text{GHz}$).

3.2.2 FEL Assembly

The schematic of the FEL resonator can be found in the middle part of Fig. 3.6. It mainly consists a drift tube, an upstream mirror, and a downstream vacuum window. A 24GHz, 10 kW magnetron signal is injected into the drift tube and propagates in the TE_{11} mode for the FEL upconversion and co-generation experiments. We chose to operate the FEL as a single pass travelling wave amplifier, which yields a stable output frequency free of the sidebands that can result from a multi-pass oscillator configuration.

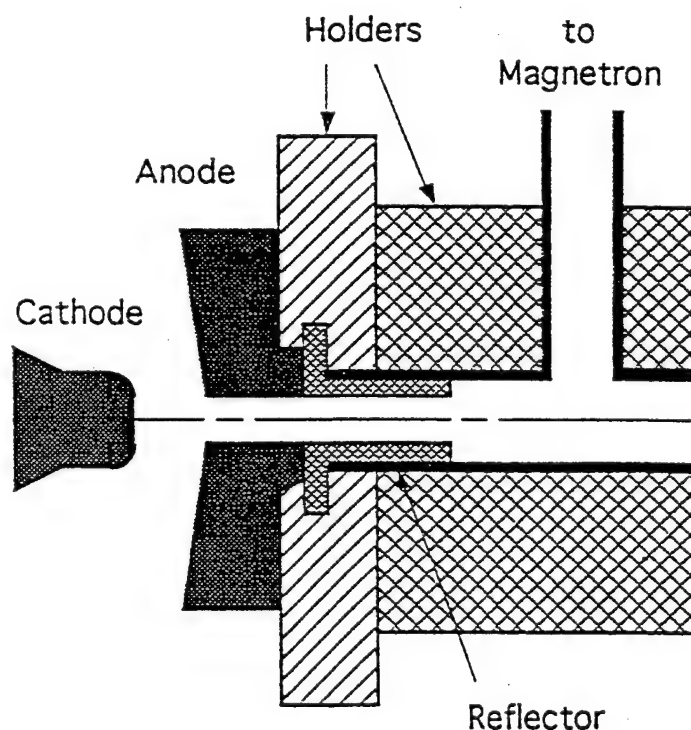


Figure 3.7 Electron beam injection region.

Fig. 3.7 describes the electron interaction region of the resonator. The 24GHz magnetron signal travels through a section of k-band rectangular wave guide (WR-42, 10.7mm x 4.3mm) in TE₀₁ mode, and is then injected into the drift tube through a launcher, after which, it travels down the cylindrical drift tube in the TE₁₁ mode. The upstream microwave mirror is a step brass reflector with a hole of 3mm diameter in the center to let the electron beam pass through. The reflectivity of this step reflector is measured to be about 75%. The inner diameter of the drift tube is 8.7 mm, which is below cutoff for all modes except TE₁₁ mode. The drift tube is 1.3m long and is made of non-magnetic stainless steel.

The downstream mirror can be quartz window if oscillation configuration is needed, or a thin film of polyethylene, which serves as a vacuum window with negligible reflection. The vacuum envelope encompasses the diode region and the entire resonator assembly. The operating vacuum pressure is below 10^{-6} Torr, and is achieved by using a standard rotary mechanical pump / oil diffusion pump combination. A piece of iron is placed underneath the end of the drift tube to bend the electron beam to the drift tube wall and terminates the interaction.

3.2.3 Constant Period Undulator

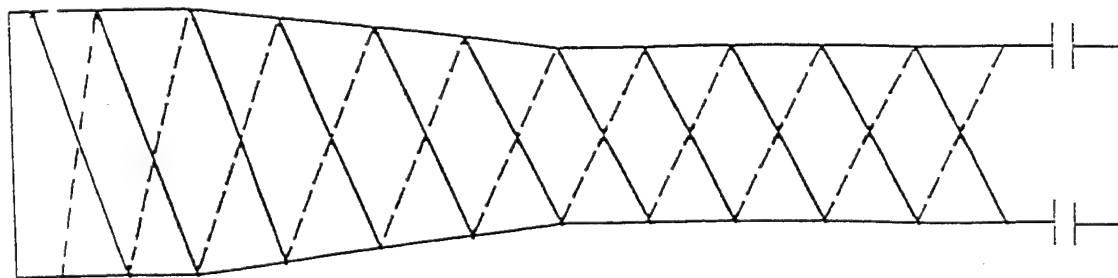


Figure 3.8 Winding of the undulator.

Figure 3.8 is the schematic of the constant period undulator and the winding. The circularly polarized magnetostatic undulator field is produced by a bifilar helically wound copper wire, which is 2.1mm in diameter (12AWG). The undulator has a constant period of 1.85cm over 1m (about 50 wiggler periods). Double helical grooves 2.1mm wide, 1.5cm deep are cut by a lathe into an insulating phenolic tube, which snugly fits over the drift tube.

The undulator is pulse-energized by an appropriately timed capacitor discharge. The two leads emanating from the downstream end of the drift tube are connected to a 10kV high voltage capacitor bank, via a thyatron switch. When the thyatron is triggered, the circuit connecting the capacitor bank and undulator is closed and a sinusoidal LC discharge current is driven through the undulator. The timing of the Marx trigger is set so as to coincide with the maximum of the undulator discharging current, which provides the maximum B_{\perp} field on axis.

The magnetic field in the undulator is measured by using a multiturn B-dot loop fixed at the end of a 66cm long glass tube. The loop probes the magnetic field on axis in the transverse direction. The loop is independently calibrated by using a Helmholtz coil with a known current, thus the absolute value for the magnetic field can be found. We discharge the capacitor bank repeatedly, as the probe is moved along the undulator axis. Fig. 3.9 shows the magnetic field structure measured at the upstream end of the undulator. The solid line is the measurement result with the probe placed in the horizontal plane, the dotted line is the result with the probe in the vertical plane. It shows the maximum achievable undulator field can be 560 Gauss with a 7kV discharge voltage. It shows an adiabatically increasing field (except the bumps at 5cm-7cm, which should be reduced) at the beginning of the undulator which is necessary for successful electron beam injection, followed by a constant amplitude field for the FEL interaction.

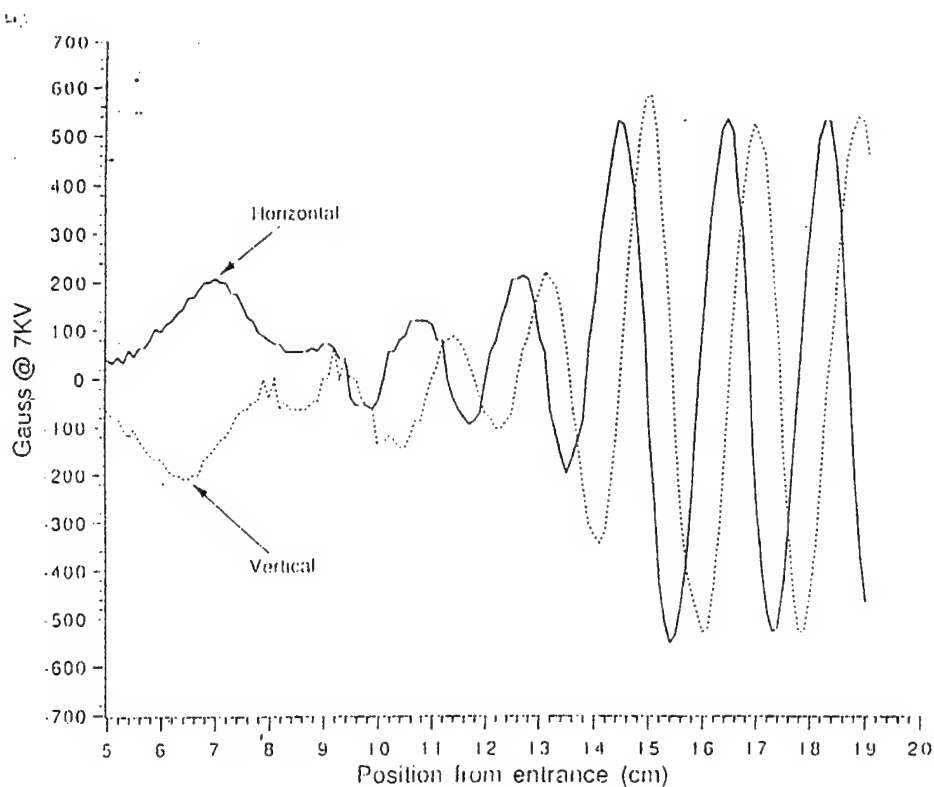


Figure 3.9 Transverse undulator field B_{\perp} profile measured at the upstream entrance of the constant period undulator, $\lambda_w = 1.87\text{cm}$.

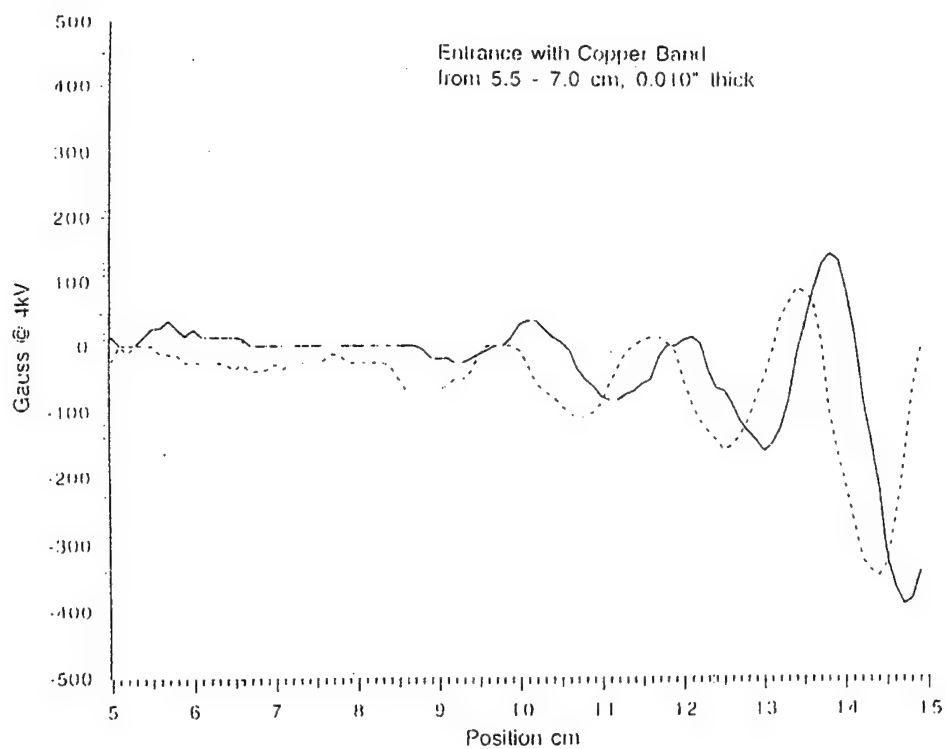


Figure 3.10 Transverse undulator field B_{\perp} profile with 4kV discharge voltage.

Fig. 3.10 is the measurement result after we put a 0.010" thick, 2cm wide piece of copper loop at position 5.5cm-7.5cm to reduce the field bumps seen in Fig. 3.9. This time the discharge voltage is 4kV instead of 7kV, since we want a low undulator field (about 250 Gauss) and corresponding small effective undulator parameter ($a_w=0.2$), so that the power gain at the 24GHz will be less than 50 to avoid unwanted feedback and oscillation.

The low undulator field has another advantage: the electron orbits in the guiding and undulator fields are stable and well-behaved upon injection into a slowly increasing undulator field. Fig. 3.11 is the computed electron transverse orbit as the electron beam enters the 1.85cm period undulator. The electron beam energy is 600keV, and the guiding field is 8800 Gauss. The undulator field increases linearly from 0 to 250 Gauss in the 8cm entry section. Fig. 3.11 shows the electron spiral orbit opens up when it enters the undulator over the few undulator periods, and orbit stays close to the axis of the undulator since the undulator field is low.

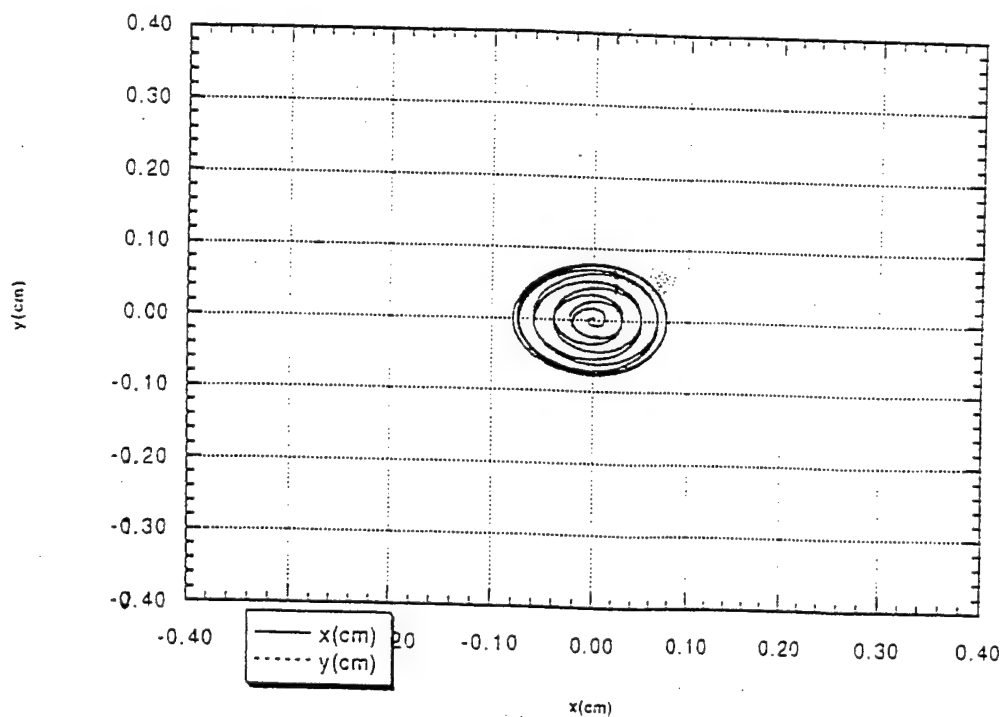


Figure 3.11 Electron transverse orbit as it enters into the 1.85 cm period undulator.

3.3 FEL Diagnostics

Fig. 3.12 shows the schematic layout of the FEL diagnostics equipments. The millimeter wave power output of the FEL is usually detected by a Schottky-barrier diode. The spectrum of the radiation is measured by the diffraction grating spectrometer. The radiation power level and time structure is monitored and measured by oscilloscopes. When measurements are taken, the detectors and oscilloscopes have to be placed in a shielded environment to avoid the RF noise.

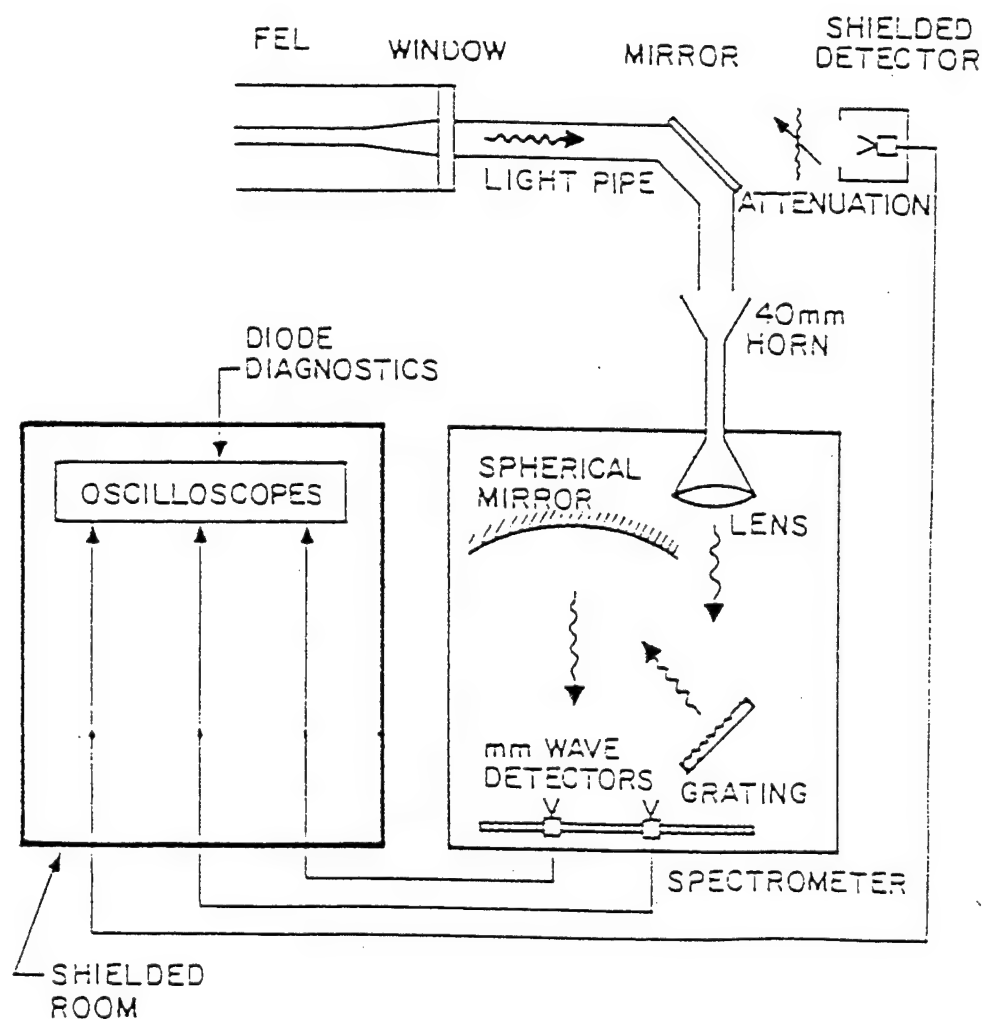


Figure 3.12 Schematic layout of the FEL diagnostics apparatus.

3.3.1 Detectors and Oscilloscopes

The microwave detectors we used are 1N26 crystal rectifiers, fed by a rectangular horn via overmoded x-band rectangular waveguide. The sensitivity of the detector is about 1V/W. The linear range of the detector is within 500mV, that means, excess radiation power may saturate the detector. Care is taken to attenuate the microwave signal sufficiently before it reaches the detector. Absorbing mats are placed in front of the receiving horns, and an adjustable attenuator is placed in the k-band waveguide input to the detector to attenuate the 24GHz signal to the linear response regime for the detector.

Several oscilloscopes are used in the experiment. For general purpose, a digital HP-54510A and TEK-2440 are used to measure the broadband microwave radiation power (signals from the shielded detectors placed along the beam line) and harmonic radiation power (signals from the detectors placed inside the spectrometer). The HP scope has a bandwidth of 250MHz and acquisition rate of 1GS/S; the TEK scope has a bandwidth of 200MHz and acquisition rate of 500MS/S. For the frequency coherence experiment, a Tektronix SCD5000 Transient Digitizer with analog bandwidth of 4.5GHz and acquisition rate of 200GS/S is used to measure the fine real-time structure of the beat wave, ie, the mixed signal of frequency-tripled 24GHz and the FEL third harmonic 72GHz.

Generally, we use more than one oscilloscope to monitor the same one shot, since each oscilloscope can only monitor two channels. Signals received by different oscilloscopes are transferred to a 486-PC computer and stored into one file. In order to show the correct timing of the signals from different oscilloscopes, we use the diode voltage to time and trigger each oscilloscope. Figure 3.13 is a typical shot where harmonic power appears: 3rd harmonic in this case. The upper trace is the 72GHz signal, the lower trace is the 24GHz signal. Also shown in this figure, for the purpose of timing, is the diode voltage trace(middle). In this shot, we use the HP scope to monitor the 72GHz signal and the diode voltage, while the 24GHz signal is monitored by the TEK scope. The horizontal scale is 50nsec/div, the diode voltage vertical scale is 200kV/div.

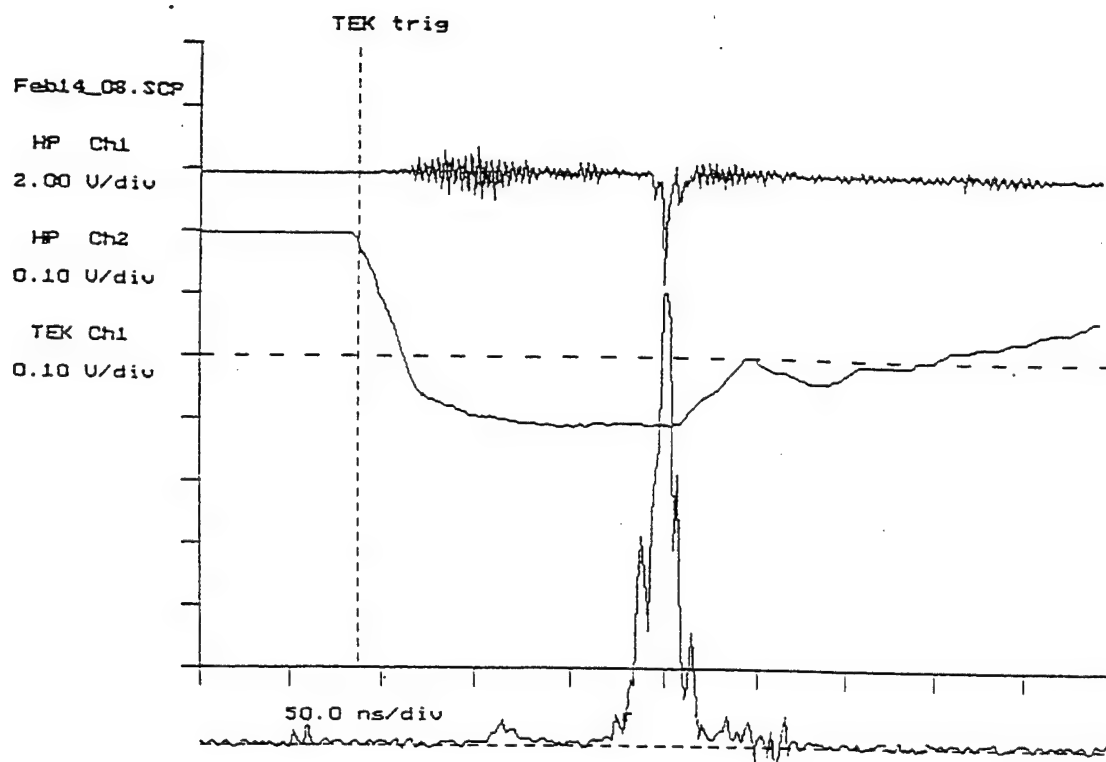


Figure 3.12 Example of harmonic (3rd harmonic) power output from FEL.

3.2mm grating $\text{GHz} = -1.14 * \text{cm} + 137.7$

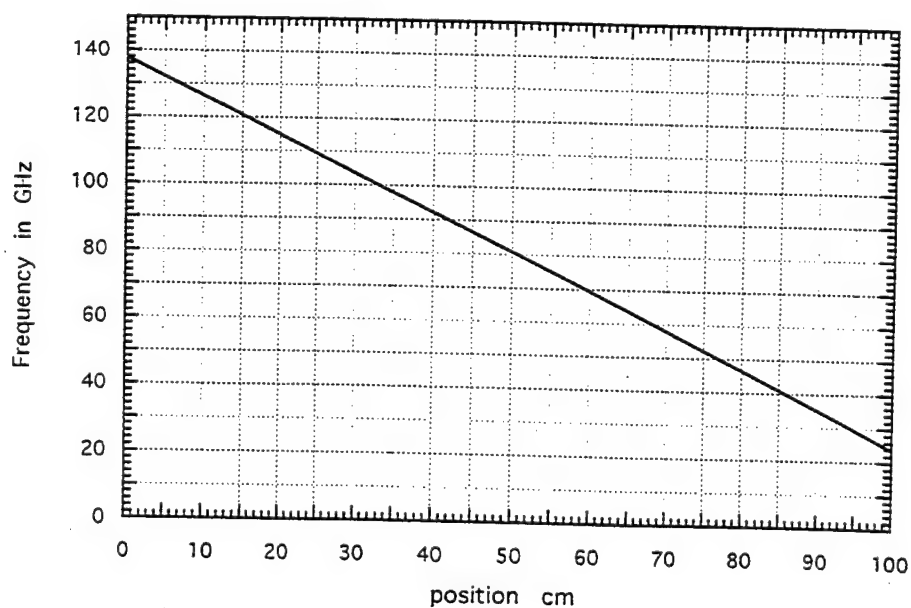


Figure 3.13 The grating calibration for the 3.2mm grating.

3.3.2 Diffraction Grating Spectrometer [1]

Radiation produced by FEL interaction is collected by a conical horn into a 1inch diameter brass light pipe and then reflected 90° to shine into the entrance of the aluminum spectrometer box. The light pipe is tapered after the 90° turn to match the 9mm inner diameter of entrance hole, whose cut-off frequency is 19GHz. The radiation is then fed into a conical horn, which is placed at the focal point of a polyethylene collimating lens. The collimated rays of radiation from the lens proceed to illuminate a diffraction grating, which is an echellete grating with a 30° blaze angle. The first order reflection is focused by a copper clad concave mirror onto the detector rail. All six sides of the spectrometer box are covered with Eccosorb foam sheets to absorb the stray radiation.

The spectrometer can be calibrated geometrically or by the 24GHz magnetron signal. In our project, we use 3.2mm period grating to scan the 3rd harmonic, 2nd harmonic and 4th harmonic, and use a 10mm grating to check the 24GHz fundamental signal. We also use a 1.3mm grating for the co-generation experiment to search the vicinity of the 7th harmonic. After one grating is calibrated, one can use the relationship: $\lambda_1/d_1 = \lambda_2/d_2$ deduced from the grating equation: $m\lambda/d = \sin \theta_i + \sin \theta_d$ to determine the corresponding position in the detector rail after changing the grating. Fig. 3.14 shows the grating calibration for the 3.2 mm grating. The resolving power is on the order of 20-50 depending on the wavelength; the detector horn will cause some linewidth broadening.

3.3.3 Harmonic Frequency Coherence Experimental Setup

In the harmonic frequency coherence experiment, we want to establish the frequency and phase relationship between the harmonic power (3rd harmonic in our case) and the 24GHz magnetron source signal. We use a subharmonic mixer, MSH-15-3NDMS, manufactured by Millitech Corporation, to frequency triple the 24GHz magnetron signal and then mix it with the 3rd harmonic signal from the FEL output. The resulting mixed

signal is monitored by an oscilloscope along with the 72GHz from a crystal detector and the 24GHz input signal.

Fig. 3.14 is the schematic layout of this harmonic frequency coherence experiment. A highly attenuated portion of the 24GHz magnetron signal travels through the WR42 waveguide and is coupled through waveguide/coax transition into the MSH-15-3NDMS subharmonic mixer. This subharmonic mixer consists of MXP-15 mixer with diplexer, it will frequency triple the 24GHz LO input signal and mix it with the 72GHz RF input signal from the FEL; the mixing IF signal is sent to the scope after it is amplified by an amplifier. Care is taken to attenuate the 72GHz harmonic signal to avoid saturating the mixer, whose working parameters are shown in Table 3.1.

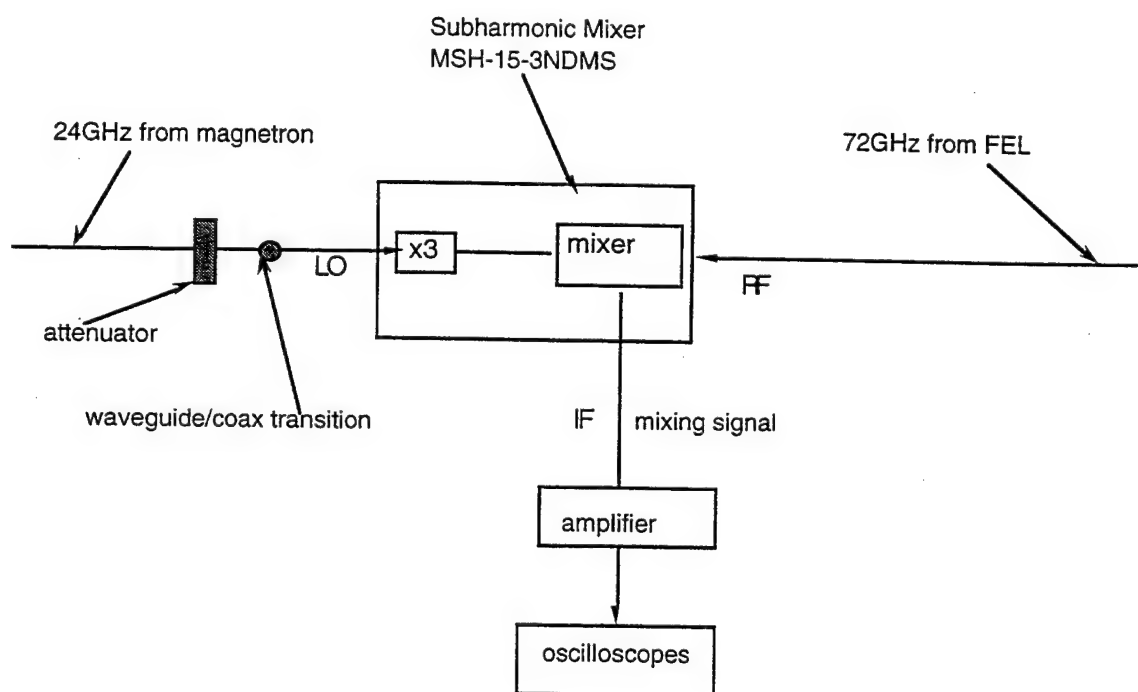


Figure 3.14 Schematic layout for the harmonic frequency coherence experiment.

Table 3.1 Working parameters of the subharmonic mixer MSH-15-3NDMS

RF frequency	72 Ghz to 75 GHz
RF input power	0 dBm maximum
LO frequency	24 Ghz (x3)
Required LO input power	+20 dBm
IF frequency	0 to 3 GHz
Harmonic number	3
Conversion loss	20 dB typical
RF connector	WR-15, MIL, F-3922/67B-008
LO & IF connectors	SMA female

References

- [1] J.A. Pasour, S.P. Schleringer, *Rev. Sci. Inst.* **48** p1355 (1977).
- [2] S.C. Chen, Doctoral Thesis, Columbia Univ. (1984) and R.H. Jackson, et. al. , *IEEE J. Quant. Elec.* **QE-19**, p346 (1983).
- [3] S.C. Chen, T.C. Marshall, *J. Quant. Elec.* **QE-21**, p924 (1985).
- [4] H.P. Freund, S. Johnston, P. Sprangle, *J. Quant. Elec.* **QE-19**, p322 (1983).

Chapter 4

Experimental Results

In this chapter, we present the experimental results of the harmonic radiation from the microwave FEL amplifier described in the previous Chapter. First we show the FEL resonant harmonic conversion experimental results: the observation of the growth of the low frequency bunching wave (24GHz signal from the magnetron) and the observation of its amplified 2nd and 3rd harmonics. We also demonstrate the coherent frequency relationship between the millimeter harmonic radiation produced and the microwave source. Then, we present our observation of appreciable seventh harmonic power, which is produced by a co-generation process.

4.1 The FEL Resonant Harmonic Conversion Experimental Results

The basic theory of the "FEL resonant harmonic conversion" is introduced in Chapter 2, now we are going to give the detailed experimental design and experimental results based on this mechanism.

4.1.1 Experimental Design

The FEL experimental design is determined by the characteristics of our microwave source, a 24GHz magnetron that provides 10kW at the input to the FEL in the circularly polarized mode that will grow along our helical undulator. We choose the TE_1 mode in a cylindrical waveguide (drift tube), which contains a 3mm diameter electron beam on its axis. The propagation and alignment of the electron beam through the waveguide were studied by taking a series of "witness plates". The witness plate records the transverse

position of the electron beam, as electron energy is released by scattering in a target that is positioned along the axis of the drift tube. The target medium is a piece of thermal paper. As shown in Fig. 4.1, the electron beam is represented by the white hole in each of the witness plates, which demonstrated the propagation of the electron beam through the waveguide. In the case of alignment, we need to adjust the drift tube to make sure the white hole (the electron beam) appears on the center of the witness plate.

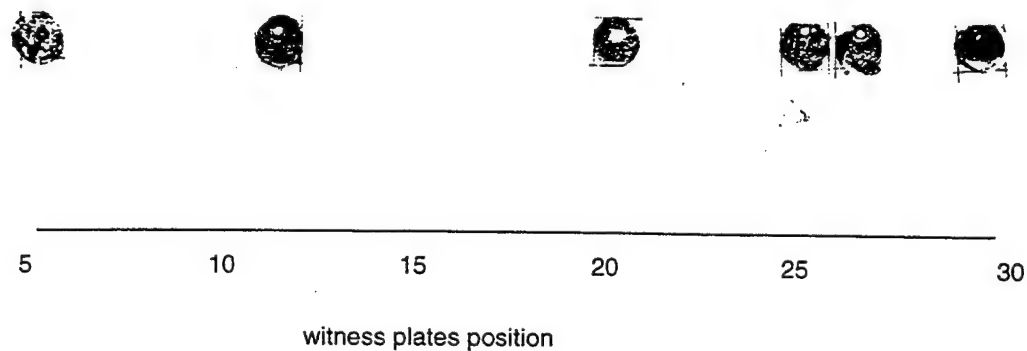


Figure 4.1 A series of witness plates versus their position along the axis of the drift tube, measured by the number of magnets counted from the end of the drift tube.

Based on formula Eq.(2.22), the diameter of the waveguide and undulator period are chosen so that exponential gain is obtained at 24GHz and at one of the harmonics, which in our case, the 3rd harmonic at 72GHz. Table 4.1, first column, shows a set of parameters which give a low frequency of 24GHz ($\omega_z/2\pi$) and a high frequency of 72GHz ($\omega_1/2\pi$), calculated by Eq.2.22, for a electron beam energy of 600keV, or $\gamma \approx 2.19$. The design was quantified by the computation of the linear gain spectrum using a single-frequency code (introduced in Chapter 5). Figure 4.2 is the computed FEL power gain versus frequency, using the parameters of Table 4.1 column I, which shows the two gain maxima that result from the two unstable roots described by Eq. 2.22. The power gain at 24GHz and 72GHz should be about 35 and 10 respectively, according to Figure 4.2.

Table 4.1 Operating Parameters of the FEL Amplifier.

	<u>Column 1</u>	<u>Column 2</u>
electron energy	600kV	600kV
low frequency FEL mode	24GHz	24GHz
high frequency FEL mode	72GHz	72GHz
undulator period	2.5cm	1.87cm
a_w , undulator parameter	0.2	0.2
guide field	0G	8800G
TE_1 cutoff frequency	18.4GHz	20.7GHz
electron beam current	~100A	~100A
electron beam diameter	3mm	3mm

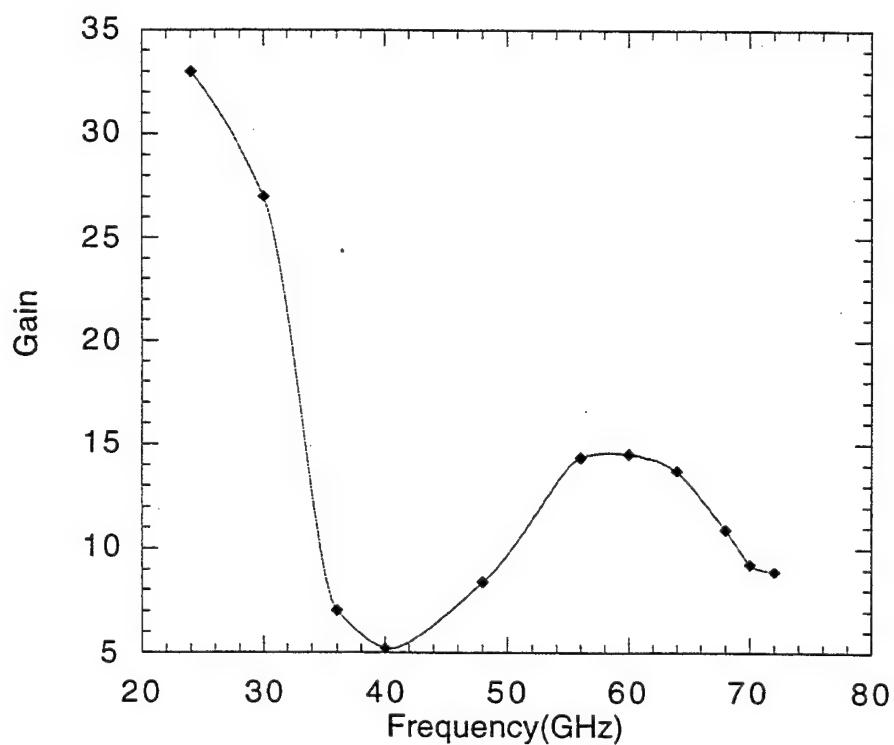
**Figure 4.2** Calculated power gain spectrum using the parameters in Column 1 of Table 4.1.

Table 4.1, second column, provides a summary of the experimental operating parameters of our Raman FEL amplifier. As expected, the two sets of parameters in Table 4.1 do not quite agree, because Eq.2.1 neglects the Raman effect, which results in a bigger effective undulator period. The Raman effect will downshift the undulator period in the following way: $\frac{2\pi}{l_{w(Raman)}} = \frac{2\pi}{l_{w(Compton)}} + \frac{\omega_p}{\gamma_1}$, based on this formular, the two columns of parameters in Table 4.1 are consistant with each other, i.e. the 2.5cm Compton undulator period corresponds to the 1.87 Raman undulator period. As we mentioned in the previous chapter, we choose a small value of undulator field (250G) and undulator parameter (0.2) to make sure the power gain at 24GHz is less than 50 in order to avoid the unwanted feedback and oscillation, and also to provide stable and well-behaved electron orbits.

4.1.2 The Power Calibration

The magnetron output (about 20kW) is matched into the waveguide by an adjustable reflector (Fig. 3.7). Approximately 10kW is launched into the right circularly polarized mode. The power radiated from the system is picked up by a receiving horn and conveyed to the screen room where there is a detector and calibrated attenuator. This permits a measurement of the gain of the 24GHz FEL.

The power calibration of the spectrometer system is approximate, since the FEL output varies over a range due to variable operating conditions. The horn-to-horn coupling is no larger than -6db (loss factor of 4) [1]. The attenuation of the spectrometer and light pipe was found to be 1/25 at 24Ghz, where a test signal was available. The insertion loss of the spectrometer at millimeter wave frequencies was found to be -12db [2]. The losses in the light pipe at frequencies ~100GHz would be higher than those at 24Ghz, about a factor of 2 higher loss at ~100Ghz due to the skin depth factor.

The broadband detector sensitivity is typically $\sim 0.1\text{V/W}$, so from the overall attenuation (a factor of 1/100-1/200) and the detector sensitivity, we can estimate the power radiated.

When the 168GHz (7th harmonic) frequencies were measured, a millimeter wave input horn was used on the spectrometer to reduce the signal and get better resolution, which introduces an extra attenuation, approximately a factor of 10.

These measurements can determine the FEL output to within an order of magnitude.

4.1.3 The Amplification of the 24GHz Wave

The FEL can be operated both as an oscillator or as an amplifier, depending on using the quartz window with reflectivity of 40% in the oscillator case, or substituting a thin polyethylene film in the amplifier case. Reflections at the end of the drift tube were minimized by use of a flared horn antenna. The system was first tested for oscillation with zero input signal from the magnetron. No oscillation signal was obtained at any frequency for undulator field less than 300G. Then we ran the system in an amplifier configuration with the magnetron on. Before we fired the system, we checked the magnetron signal on the oscilloscope, which is a $1\mu\text{sec}$ flat pulse. Since we already know the output power level of the magnetron (10kW), we can calibrate the power level of the amplified 24GHz signal by measuring the vertical amplitude (in Volts) of the signal on the oscilloscope. We put enough attenuation to lower the magnetron signal power level appearing on the oscilloscope to make sure not to saturate the oscilloscope by future amplified signal.

At the beam energy of 600kV, we observed the amplified 24GHz signal with power gain of about 10-40 for the small undulator field of 250G. Fig. 4.3 is a typical shot, which shows the amplified 24GHz signal with a power gain of ~ 20 . The calibrated diode voltage at which this effect occurs is about 600kV, but because of the space charge depression at the electron beam and the calibration accuracy, we estimate the beam energy to be $\gamma \approx 2.1$. The 24GHz signal is obtained from the magnetron which must be timed to

the firing of the pulse-line accelerator and the pulsed undulator current. The magnetron signal is the flat pulse with an amplitude of 0.1V which appears earlier than the amplified 24GHz signal pulse.

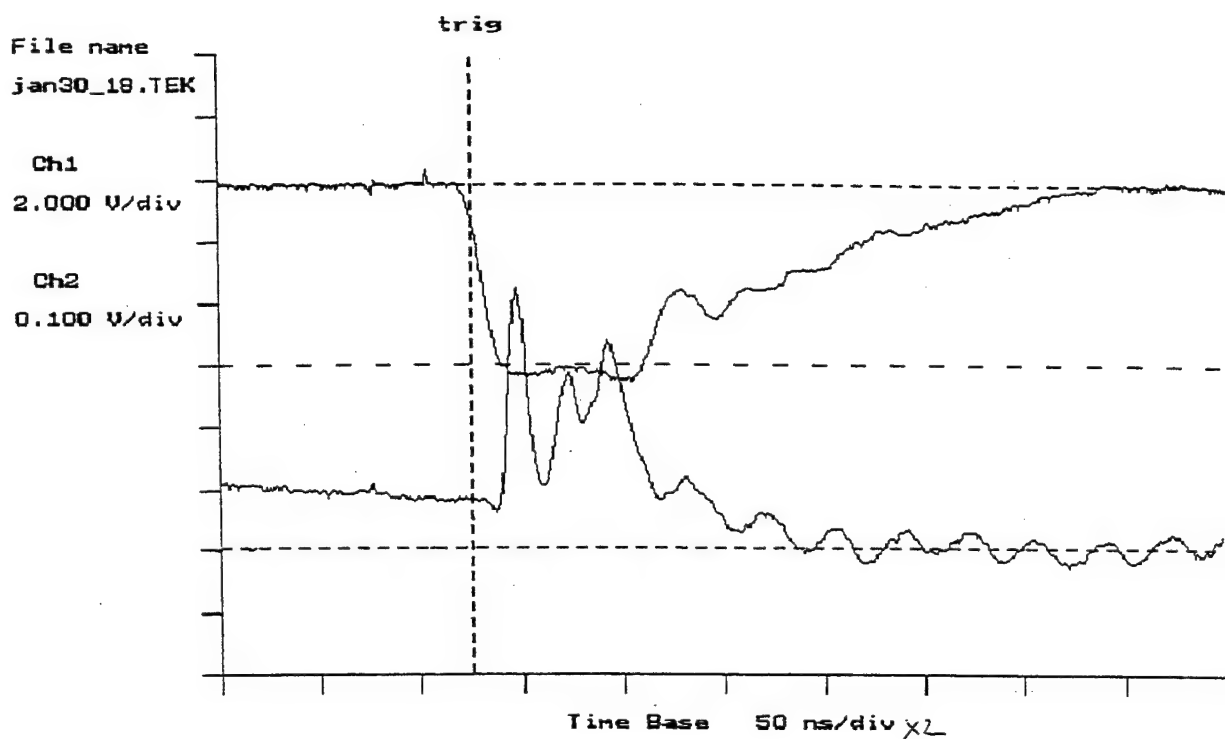


Figure 4.3 The amplified 24GHz signal (lower trace) and the diode voltage (upper trace).

4.1.4 Observation of the Harmonic Radiations

At the same time of observation of amplified 24GHz bunching wave, we found that the third harmonic is also produced. Fig. 4.4 shows typical data: the 72GHz wave appears when the 24GHz wave is amplified, but not otherwise. Also shown in this figure, for purpose of timing, is the diode voltage trace. These signals are obtained from HP and TEK

oscilloscopes which observe the same shot. Note the 72GHz emission occurs coincident with the same point on the diode voltage history as the peak 24GHz signal.

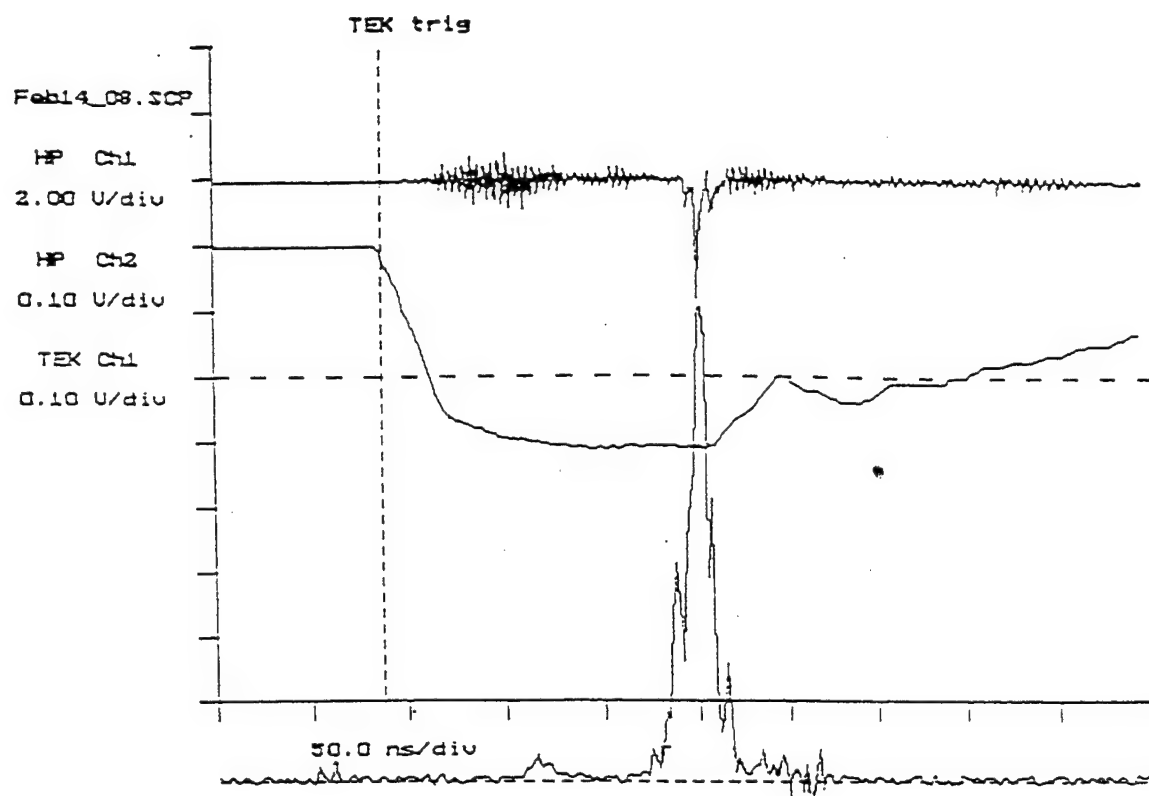


Figure 4.4 Time dependent signals of power emitted at 24GHz (below) and 72GHz (above) from the FEL. Also shown is the diode voltage signal (middle).

A scan of the millimeter power spectrum covering the first three harmonics is shown in Fig. 4.5, in which the data points represent average of the peak power of several shots. The performance of the device is such that there is appreciable fluctuation due to the varying beam conditions, and this amounts to a standard deviation of about $\pm 40\%$ on the data points. As shown in Fig. 4.5, harmonic emissions were also observed at the second

and at the fourth. The third harmonic power output was found to be greater than the second, and both are much greater than the fourth. If the interaction were non-resonant, then the power of the harmonics should fall off very rapidly[3] with increasing harmonic number. The experiments show very clearly that no harmonic power is obtained unless there is appreciable gain for the 24GHz wave.

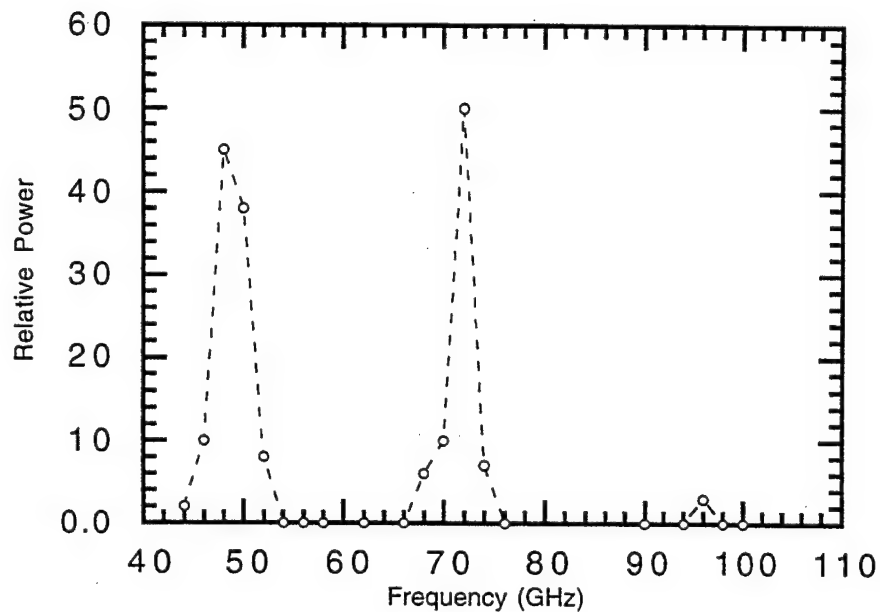


Figure 4.5 A scan of the millimeter power spectrum of the 24GHz FEL amplifier, with the electron beam on the axis.

4.1.5 The Harmonic Frequency Coherence Experiment

The harmonic frequency coherence experimental set-up described in Chapter 3 was used to determine the frequency relationship between the third harmonic (72GHz) radiation signal and the magnetron (24GHz) source signal. We used two sets of amplifier /oscilloscope combinations to monitor the mixing signal. One combination is the 4.5GHz bandwidth TEK SCD5000 transient digitizer and the 2-4GHz bandwidth amplifier (gain of 34db), the experimental result is shown in Fig. 4.6. As shown in Fig. 4.6, the 2-4GHz frequency beat wave amplitude is very small. We need a narrower bandwidth amplifier to reproduce the mixed signal pulse shape waveform, so we changed to a 0-500MHz bandwidth amplifier (gain of 16db) and the 200MHz bandwidth TEK scope combination; the corresponding experimental result is shown in Fig. 4.7. Fig. 4.7 shows a much bigger beat wave signal (the lower trace), which suggests that the beat wave frequency is in the order of zero. For our experiment, due to the finite pulse times $\sim 20\text{nsec}$, the difference between "zero" and 50Mhz beat wave cannot be resolved.

In both cases, in addition to monitoring the beat signal envelope of FEL third harmonic mixed with magnetron tripled frequency, we also monitored the 24GHz power gain and the 72GHz signal amplitude obtained by a Schottky-barrier crystal detector. The 72GHz signals were obtained from two separate horns, located in the spectrometer where the third harmonic would appear. One horn feeds the tripler/mixer, while the other goes directly to a crystal detector. The diode voltage trace is shown for the purpose of timing. The appearance of a coincident mixer output shows that there is a stable frequency relationship between the 24GHz magnetron input power which drives the FEL bunching and the third harmonic FEL output power.

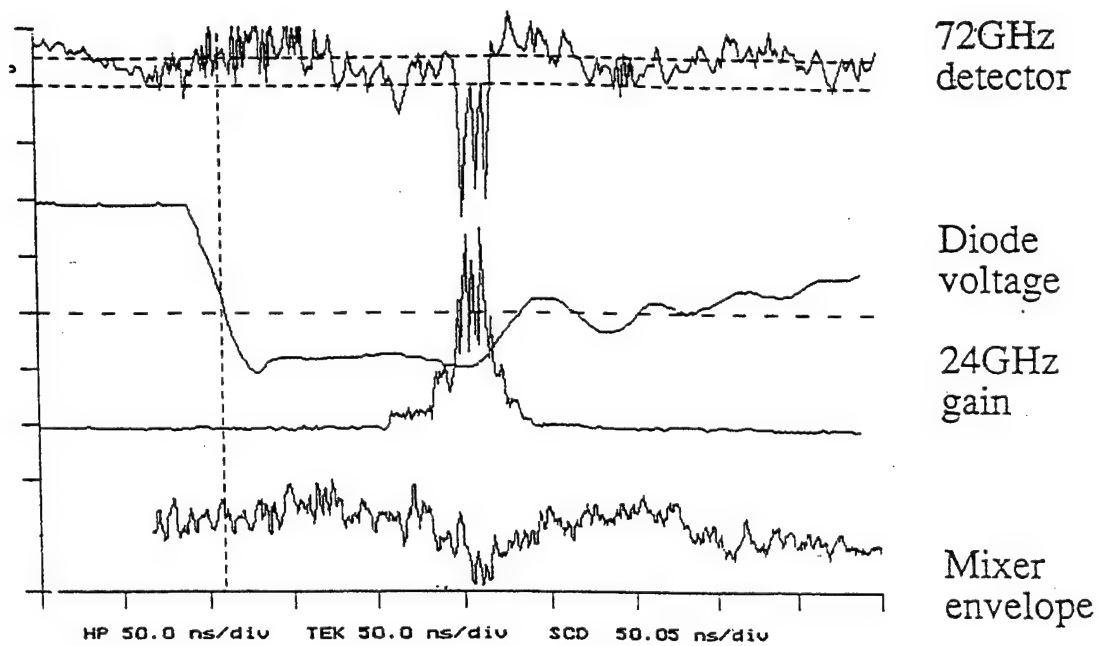


Figure 4.6 The harmonic frequency coherence experimental result, the mixing signal is obtained from SCD scope with the 4GHz amplifier.

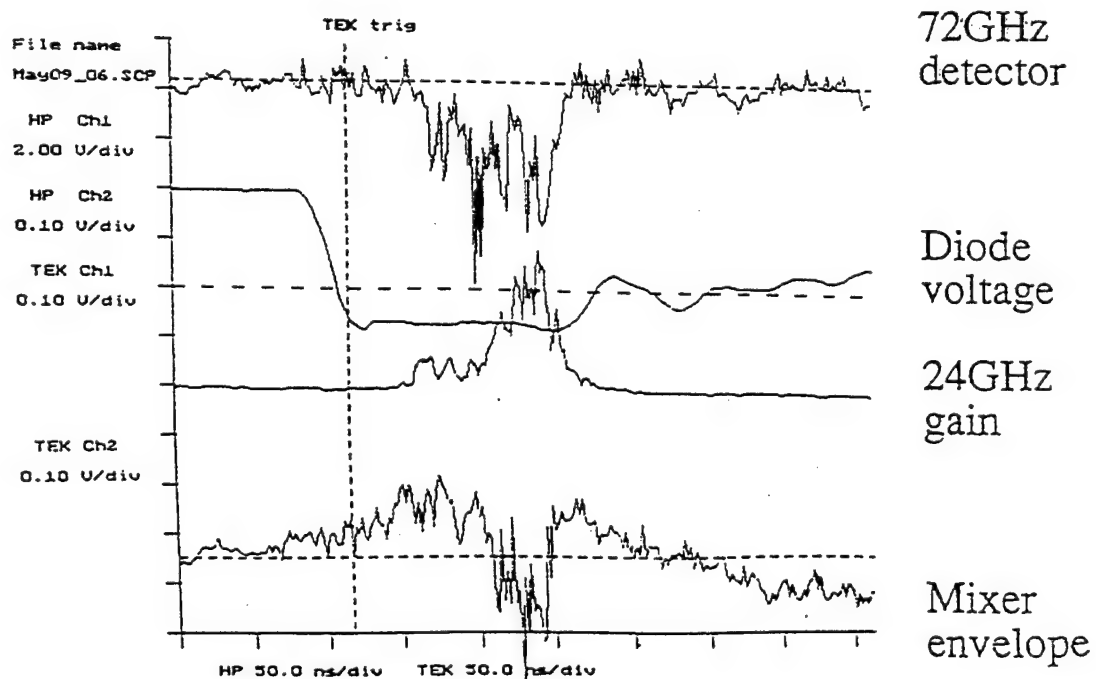


Figure 4.7 The harmonic frequency coherence experimental result, the beat wave signal is obtained from the TEK scope with the 500MHz amplifier.

4.2 The Observation of the Seventh Harmonic Emission

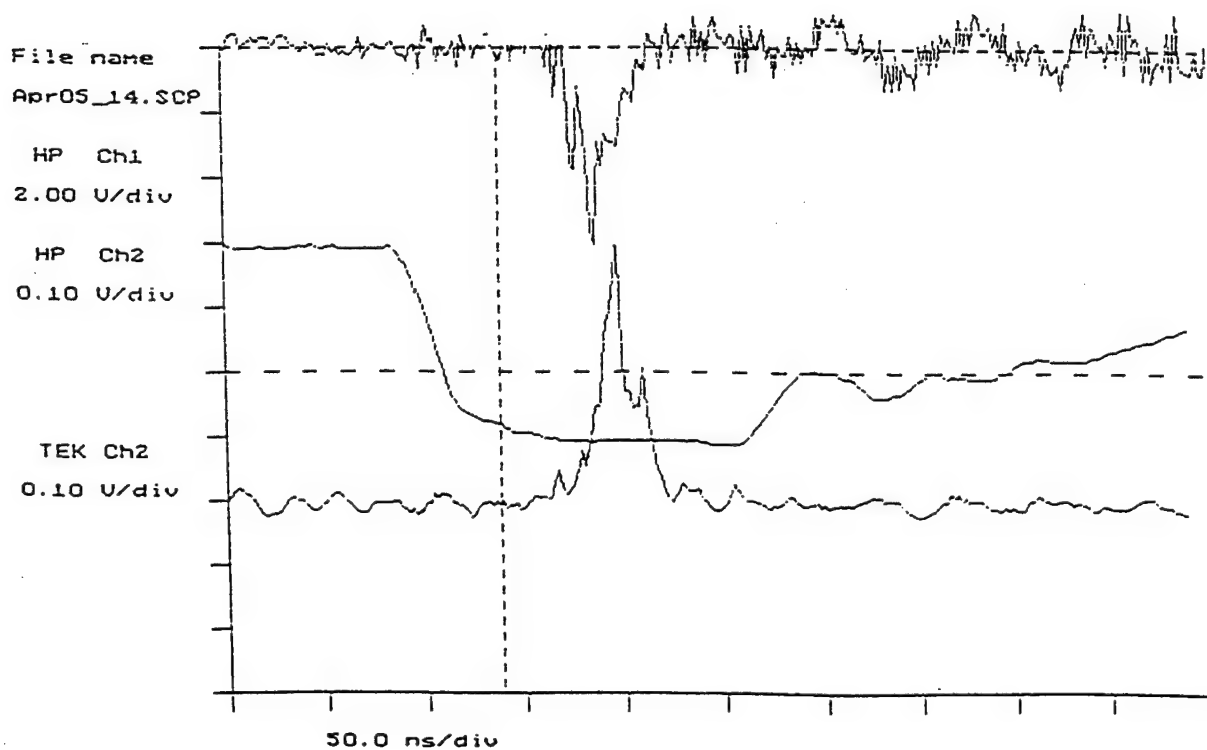


Figure 4.8 A typical shot with the seventh harmonic 168GHz emission (upper trace), the amplified 24GHz wave (lower trace), and the diode voltage (middle trace)

Figure 4.8 is a typical shot showing the emission of appreciable seventh harmonic 168GHz power, in which the seventh harmonic signal level is $\sim 1\text{kW}$, whereas the 24GHz signal is amplified to $\sim 400\text{kW}$, much less than saturation (a few MW). The seventh harmonic emission is obtained only when we have appreciable gain for the 24GHz FEL wave and when there was a misalignment of our system. The electron beam was moved about 2mm off the waveguide axis measured at the end of the wiggler, which was monitored by taking a series of "witness plates".

As we stated in Chapter two, the seventh harmonic is not a “resonant FEL interaction” and its appearance should depend on two special conditions. The first is that the temporal and spatial spectrum of the seventh harmonic electromagnetic wave must move at very nearly the same wave velocity as the temporal and spatial spectrum of its electron current source, the latter is set up by the seventh temporal harmonic of the bunching caused by the amplified TE_{11} 24GHz wave. The EM wave in question that satisfies this constraint is the TE_{72} mode of the cylindrical waveguide [4], since this wave has nearly the same wave refractive index as the TE_{11} wave at 24GHz. Also, since the TE_{72} mode has zero transverse E-field on-axis, the electron beam has to be moved off-axis to overlap one of the electric field maxima of the TE_{72} wave.

By satisfying the above two conditions, i.e. moving the electron beam off-axis and amplifying the 24GHz microwave signal, we observed the seventh harmonic signal in this device for electron beam energy as low as 400kV. As shown in Fig.4.9, the seventh harmonic emission and the amplified 24GHz signal appears when the diode voltage is only about 400kV. Using the single frequency code we used in Fig. 4.2, but changing the electron beam energy to 400kV, we get the computed gain curve for this “tangent case” (described in section 2.2.2), now there is only one intersection between the beam line and the waveguide dispersion curve. As shown in Fig. 4.10, there is still gain at 24GHz for this lower beam energy.

This seventh harmonic output is potentially an attractive alternative for a CW FEL which has to generate appreciable power at ~ 2 mm wavelength for plasma CW electron cyclotron heating since we have obtained this radiation for electron beam energy as low as 400kV, and DC power source with this voltage are available commercially.

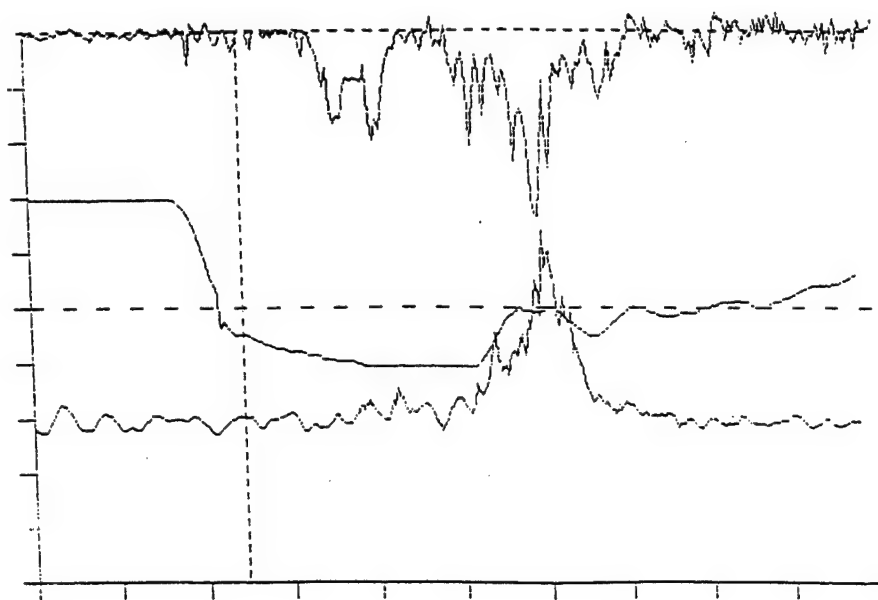


Figure 4.9 The 168GHz converted power (above) and 24GHz amplified power (below), obtained when the diode voltage (middle) is only about 400kv.

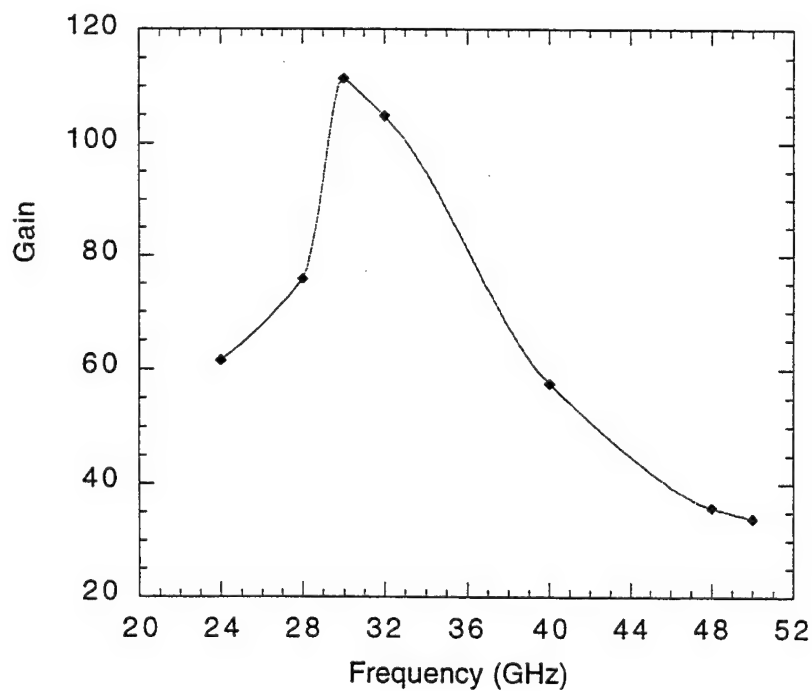


Figure 4.10 Computed FEL gain versus frequency, for beam energy of 400kV.

We did a more complete power scan which covers harmonics number from 2 to 8 for the electron beam off-axis case. Experiment shows that radiations were observed in the vicinity of the seventh harmonic, but there is no radiation at either the second harmonic or the third harmonic. On the other hand, after we moved the electron beam back on-axis, we did reproduce a certain amount of the third harmonic, a smaller amount of the second harmonic and even smaller amount of the fourth harmonic, but the radiation output for harmonics greater than five is zero with the electron beam on-axis. By adding those new data points obtained from the beam off-axis case into Fig. 4.4, we can get a complete power spectrum scan which covers the experimental results about the harmonics from 2 to 8, with both the electron beam on-axis and off-axis. As shown in Fig. 4.11, the seventh harmonic output power was found to be the biggest and the third harmonic output power was the second biggest.

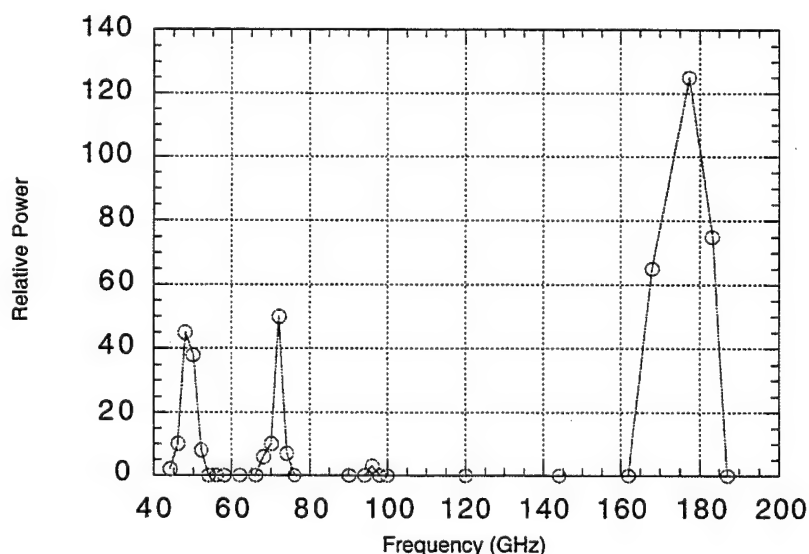


Figure 4.11 Millimeter power spectrum scan for the 24GHz FEL amplifier, covering harmonics 2 - 8; beam is off-axis for harmonics >5, signals for the 7th harmonic and harmonics >5 are zero for on-axis beam.

4.3 The Oscillator Experiments

Using the Columbia FEL configured as a traveling-wave amplifier, we have amplified the 10kW 24GHz microwave input signal (from the magnetron) to ~400kW level, and obtained ~1kW emission of the seventh harmonic, most likely from the TE₇₂ mode and less than 1kW third harmonic emission, most likely from the TE₁₁ mode. According to the numerical computational results (shown in Fig. 5.6), it is necessary to have either a larger input microwave power or a higher-gain system in order to get higher harmonic output power. The figure shows that the harmonic power output is very sensitive to the output microwave power, which suggests that we operate the system in a way to make the microwave output power near saturation level so that the harmonics of the bunching will be larger [3].

Since there is no higher microwave source power available, and it is not very practical to expand the length of the interaction region of our FEL amplifier either, we tried to operate the system in a oscillator configuration in order to saturate the microwave output power and convert more harmonic output power. However, the experiment did not show obvious improvement for the power level of the harmonics, even though we did obtained a bigger microwave output signal. This result suggests that there might be more complicated processes going on in an oscillator configuration, which should be studied further. Among these, there might be a more random beam bunching pattern, which would not favor stronger harmonic output.

4.4 The current wave-form and its effects

The current in the beam is obtained by field emission from the cold cathode. In Fig. 4. 12[5], we find the current has rapid and non-reproducible variations. These account for the finite pulse widths and shapes obtained for the amplified 24GHz signal as well as the harmonics.

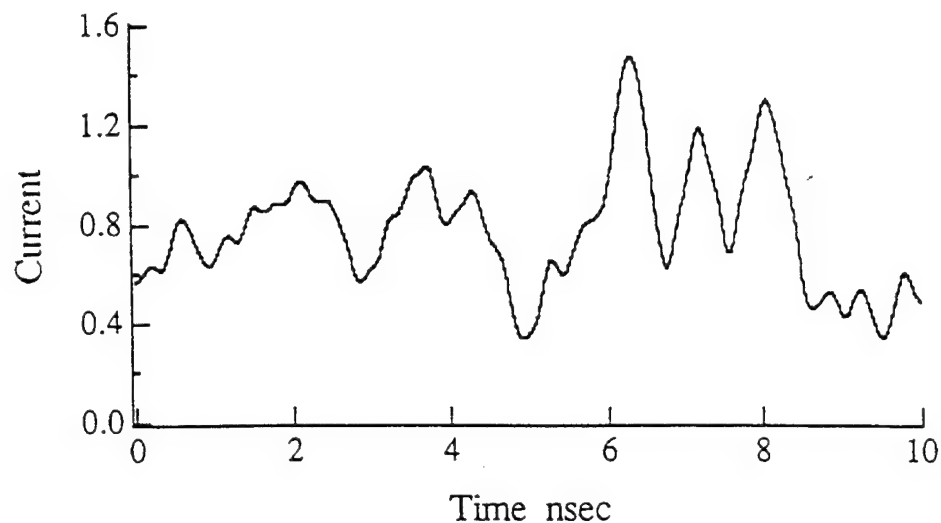


Fig. 4.12 Current (arbitrary units) drawn by a low inductance coaxial wire probe in the electron beam; the current pulse is 150ns long, but this shows only a 10ns “window”. The average current is about 100A (as determined by a Faraday cup). Note the three pulses of current between 6 and 8ns.

References:

- [1] M.A. Heald and C.B. Wharton, “Plasma Diagnostics with Microwaves”, p329, John Wiley, NY (1965).
- [2] R. Gilgenbach, Doctoral Thesis, Columbia Univ. (1978).
- [3] Y. -P. Chou and T.C. Marshall, *Nucl. Instrum. Meth. in Phys. Res.* **A318**, p528 (1992).
- [4] C.Wang, J.L. Hirshfield and A.K. Ganguly, *Phys. Rev. Lett.* **77**, p3819 (1996).
- [5] LiYi Lin et al, *Nucl. Instrum. Meth. in Phys. Res.* **A341**, p265 (1994).

Chapter 5

Numerical Model and Simulation Results

To study the coupling between the harmonically related waves, we need to solve numerically the set of coupled FEL partial differential equations we developed in Chapter 2. In this chapter, we will show the algorithm to numerically solve the equations, and the numerical simulation results.

5.1 The Numerical Model for the 2-wave Compton FEL

The equation set (Eq.(2.29), (2.31), (2.32) and (2.33)) we derived in section 2.2.3 are first-order parabolic partial differential equations with respect to time t and space z . We solve them numerically in the following way:

First we introduce two new variables x and y as

$$x = A \left(t - \frac{z}{v_{g2}} \right), \quad y = A \left(\frac{z}{v_1} - t \right) \quad (5.1)$$

where $A = \left(\frac{1}{v_1} - \frac{1}{v_{g2}} \right)^{-1}$ and v_{g2} is the group velocity of ω_2 , so that $\frac{\partial}{\partial z} + \frac{1}{v_1} \frac{\partial}{\partial t} = \frac{\partial}{\partial x}$, $\frac{\partial}{\partial z} + \frac{1}{v_{g1}} \frac{\partial}{\partial t} = \frac{\partial}{\partial y} \left(\frac{1}{v_1} - \frac{1}{v_{g1}} \right) A + \frac{\partial}{\partial x} \left(\frac{1}{v_{g1}} - \frac{1}{v_{g2}} \right) A$, and $\frac{\partial}{\partial z} + \frac{1}{v_{g2}} \frac{\partial}{\partial t} = \frac{\partial}{\partial y}$. Then the FEL equations can be rewritten as:

$$\frac{\partial \theta_{2j}}{\partial x} = \overline{k_{w2}} \left(1 - \frac{\overline{\gamma_{r2}^2}}{\gamma_j^2} \right) \quad (5.2)$$

$$\frac{\partial \gamma_j}{\partial x} = - \frac{a_w}{\gamma_j v_{1j}} \left[\omega_1 a_{s1} \sin(\alpha \theta_{2j} + \phi_{1j}) + \omega_2 a_{s2} \sin(\theta_{2j} + \phi_{2j}) \right] \quad (5.3)$$

$$\left[\frac{\partial}{\partial y} + \left(\frac{\frac{1}{v_{g1}} - \frac{1}{v_{g2}}}{\frac{1}{v_1} - \frac{1}{v_{g1}}} \right) \frac{\partial}{\partial x} \right] a_1 = i \left(\frac{\frac{1}{v_1} - \frac{1}{v_{g2}}}{\frac{1}{v_1} - \frac{1}{v_{g1}}} \right) \frac{\omega_p^2 a_w}{2c^2 k_1} \left\langle \frac{e^{-i\alpha\theta_1}}{\gamma} \right\rangle \quad (5.4)$$

$$\frac{\partial a_2}{\partial y} = i \frac{\omega_p^2 a_w}{2c^2 k_2} \left\langle \frac{e^{-i\theta_2}}{\gamma} \right\rangle \quad (5.5)$$

This complete set of equations can then be integrated by computer with finite difference methods. Note that Eq. (5.2) , (5.3) are ordinary differential equations with respect to x, and Eq. (5.5) is ordinary differential equation with respect to y. Thus the new variables chosen are such that electrons move long lines of constant y, and the wave ω_2 is propagated along lines of constant x. The harmonic wave ω_1 is integrated along its characteristic curve in the x-y plane:

$$x - \frac{\frac{1}{v_{g1}} - \frac{1}{v_{g2}}}{\frac{1}{v_1} - \frac{1}{v_{g1}}} y = \text{const.} \quad (5.6)$$

which is a straight line with a slope of $\frac{\frac{1}{v_1} - \frac{1}{v_{g1}}}{\frac{1}{v_{g1}} - \frac{1}{v_{g2}}}$. Hence wave ω_1 starting from the

same initial point will terminate at different point at a later time (shown in Fig. 5.1). Interpolations are thus necessary to calculate the field a_1 if this line does not fall at the grid point where a_1 is needed for computing the electron motion (Eq.5.3, 5.2) , and similar interpolations are needed to calculate the electron energy γ_j and the phase θ_j for computing the field a_1 (Eq. 5.4). Our numerical scheme for integrating these equations is a fourth order Predictor-Corrector method [1].

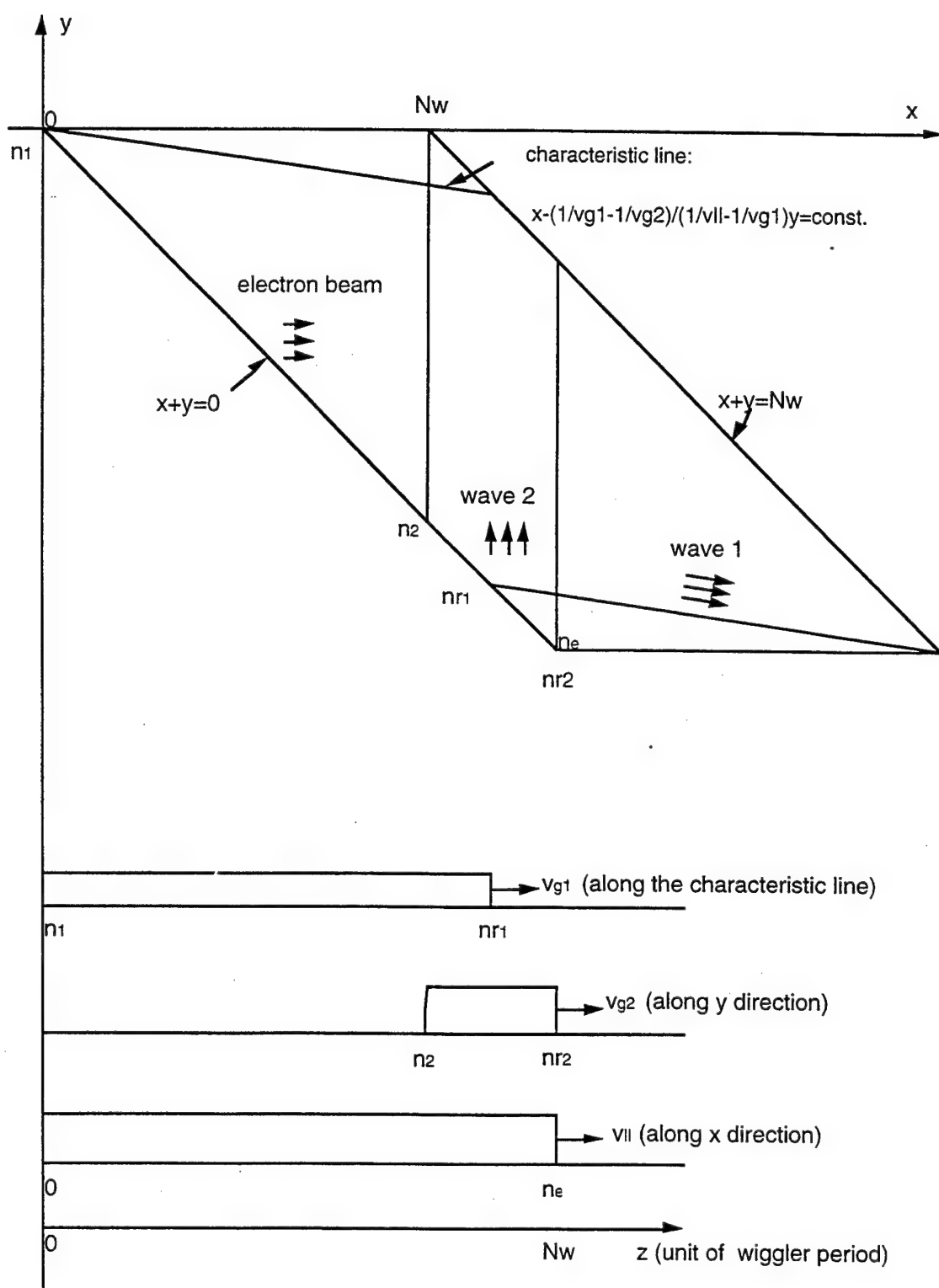


Figure 5.1 Computational grid for the 2-wave numerical model.

Also shown in Fig. 5.1 are the initial and boundary conditions of the electron beam and the two waves. The spatial distribution of simulation electrons has a rectangular profile, the electrons are taken to be monoenergetic, and at the undulator entrance $z = 0$, they are uniformly distributed inside the beam length $(0 - n_e)$ with 100 simulation electrons per wiggler period. For each wavelength-size strip of particles, the relative phase location of the electrons with respect to the radiation field of ω_2 is uniformly distributed between $-\pi$ to π . The input 24GHz radiation pulse ($n_2 - n_{r2}$) is "seeded" inside the electron beam, with its initial amplitude a_{s0} . And the harmonic wave ω_1 ($n_1 - n_{r1}$) starts from a small initial amplitude.

In the simulation, the FEL behaves as a traveling wave amplifier, with the operation parameters given by Column 1 in Table 4.1. The finite radial size of the electron beam is accounted for in the code by using a multiplicative "filling factor" for the radiation current term on the right hand sides of Eq. (5.4) and (5.5). While this can be estimated from geometry, it is also a convenient parameter to adjust the gain of the 24GHz wave so that it corresponds to our experimental results. For the output format of the computational results, the electron beam pulse and the two radiation pulses (each taken to be flat-topped) are plotted as a function of the variables of x and y , which imply two moving "windows", the former at v_{g2} and the latter at v_1 respectively; both are scaled in the unit of wiggler period.

5.2 Simulation Results Related to the Third Harmonic

The nonlinear interaction of the two waves causes a variety of effects which are too varied to be summarized here. However, we will show some simulation results relevant to our experimental results.

Fig. 5.2 shows the peak power growth along the undulator of the 24 and 72GHz ($\alpha = 3$, the 3rd harmonic) waves. The 24GHz wave starts from an initial signal of several kW ($a_{s2}^2(0) = a_{s0}^2 = 10^{-5}$) in the right circular polarized mode, and the 72GHz wave starts from few watts of initial signal level ($a_{s1}^2(0) = 10^{-11}$). At the end of the undulator (after 40

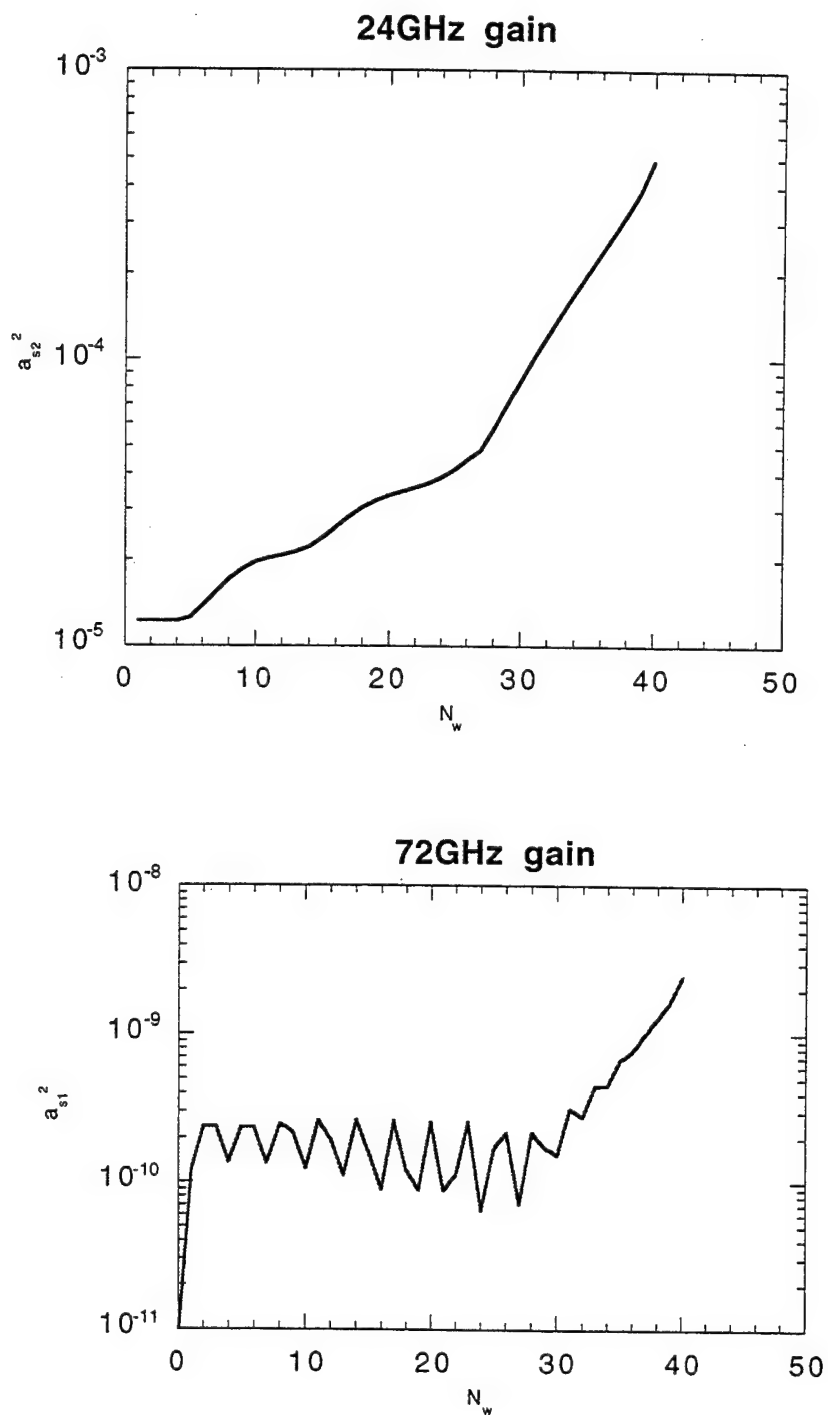


Figure 5.2 Power growth of the 24 GHz (above) and 72GHz (below) waves along the undulator computed from theory using the parameters of Column 1 of Table 4.1.

wiggler periods) , a few hundred watts is obtained at 72GHz ($a_{s1}^2 = 2.0 \times 10^{-9}$) , together with a power gain of 50 at 24GHz ($a_{s2}^2 = 5.0 \times 10^{-4}$). Those simulation results are quantitatively consistent with our experimental results (Fig. 4.4). Fig. 5.2 also shows that the harmonic power begins its rapid growth only when the bunching produced by the microwave develops a substantial harmonic component, until then (at ~ 30 wiggler periods) , the bunching harmonic and its wave amplitude remain small and "noisy" [2].

Fig. 5.3 shows the pulse shapes (amplitude versus time) of the 24GHz wave and 72GHz at the end of the undulator. The two waves move with their own group velocities, ($v_{g1} = 0.97c$ and $v_{g2} = 0.51c$), and the electron beam axial speed is : $v_i = 0.88c$. So the 24GHz radiation pulse slips backward into the electron beam from right to left, and the 72GHz radiation pulse slips forward into the electron beam from left to right, this slippage effect can be also seen in the computational grid graph (Fig.5.1). As shown in Fig.5.3, the radiation pulses appear coincidentally with each other, which is consistent with our experimental observation (Fig. 4.4).

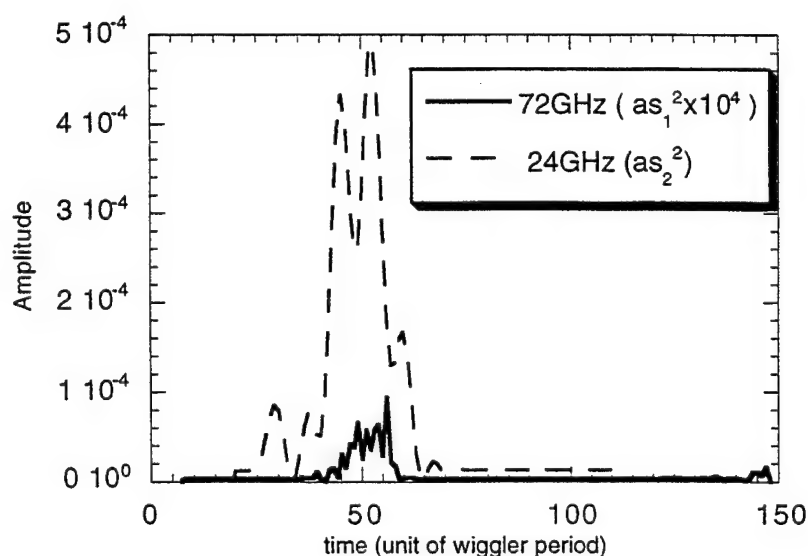


Figure 5.3 The radiation pulses of 24GHz and 72GHz waves at the end of undulator.

In the above simulation run, we use a filling factor of 0.2 in order to get the same power gain (~ 40) at 24GHz. If we increase the filling factor from 0.2 to 0.35 and keep all other parameters the same, we get the results shown in Fig. 5.4. At the end of the undulator, the 24GHz wave has a power gain of 400, and the 72GHz wave grows from initial signal level of $a^2_{s1}(0) = 10^{-11}$ to $a^2_{s1} = 1.0 \times 10^{-7}$.

If we keep the filling factor as the same (0.2), but start the 24GHz wave from a higher initial signal level, from $a^2_{s2}(0) = 10^{-5}$ to $a^2_{s2}(0) = 10^{-4}$, then we get the results shown in Fig. 5.5. This time, the power gain of 24GHz at the end of undulator is still about 40, but with a higher final signal level, and the 72GHz wave grows from $a^2_{s1}(0) = 10^{-11}$ to $a^2_{s1} = 1.0 \times 10^{-7}$.

In order to compare these three cases, we combined Fig. 5.2, Fig. 5.4 and Fig. 5.5 into one figure (Fig. 5.6), by converting the vertical axis label to the corresponding power level. In this figure, the solid line pair represents the Fig. 5.2 case, which is the case consistent with our experiment; the dotted line pair represents the case of Fig. 5.4, which gives a power gain of 400 at the 24GHz by using a bigger filling factor; the dashed line pair represents the Fig. 5.5 case, which starts the 24GHz wave from a higher initial signal level. By comparing these results, one finds that: in order to get harmonic power of tens of kW, it is necessary to have either a large input microwave power or a high-gain system; the requirement is that the device achieve a microwave power output near saturation level so that the harmonics of the bunching are large [2]. Since a gain of 400 at 24GHz would cause the device to oscillate, the way to improve the harmonic output is by increasing the input microwave power. Fig. 5.6 shows that the harmonic output is very sensitive to the output power of the microwave; we find that as much as 70kW of third harmonic can be produced if the computation is carried further along to 50 wiggler periods.

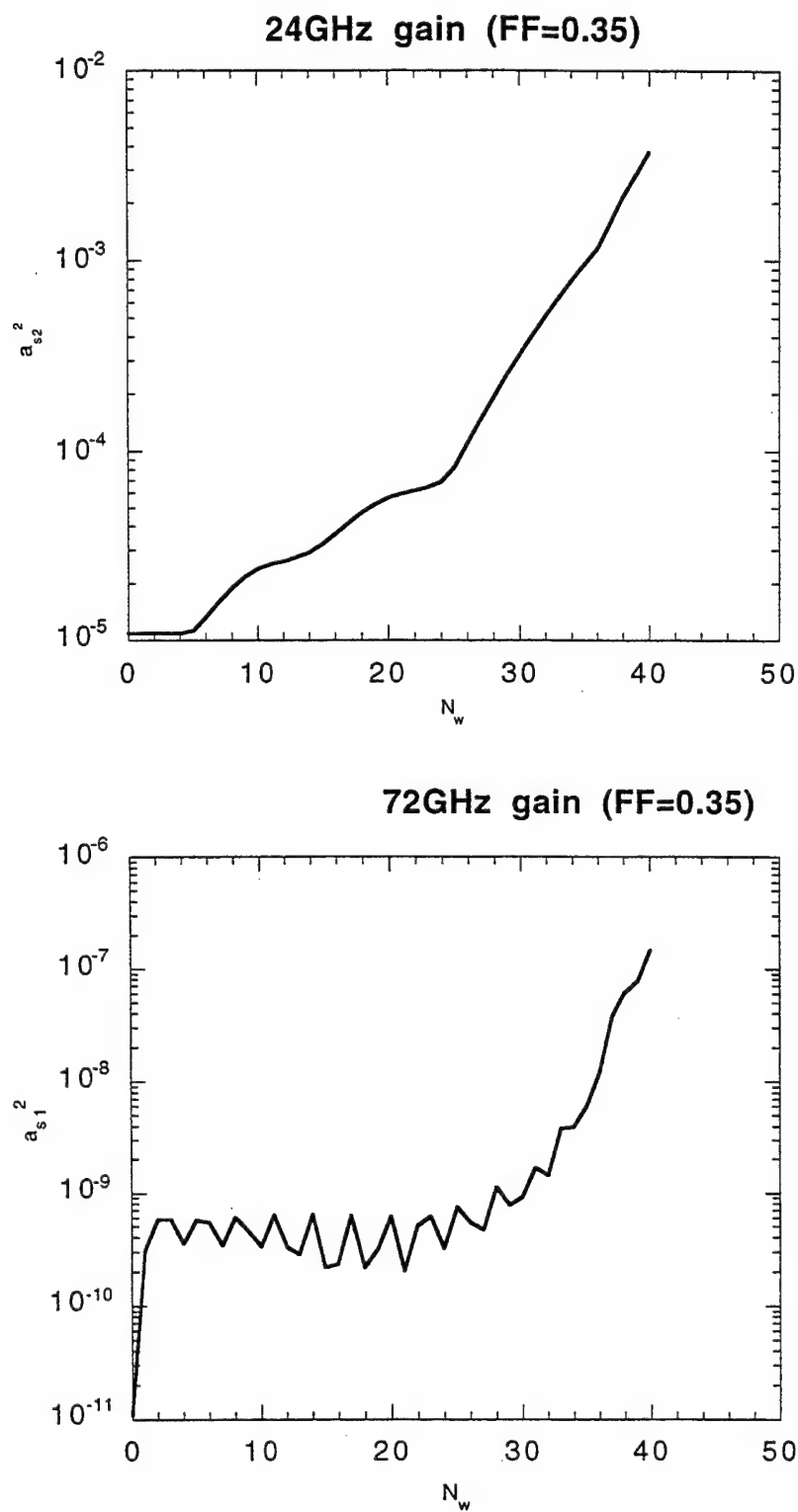


Figure 5.4 The peak power growth of 24GHz (upper) and 72GHz (lower) waves along the undulator with a power gain of 400 at 24GHz at the end of the undulator.

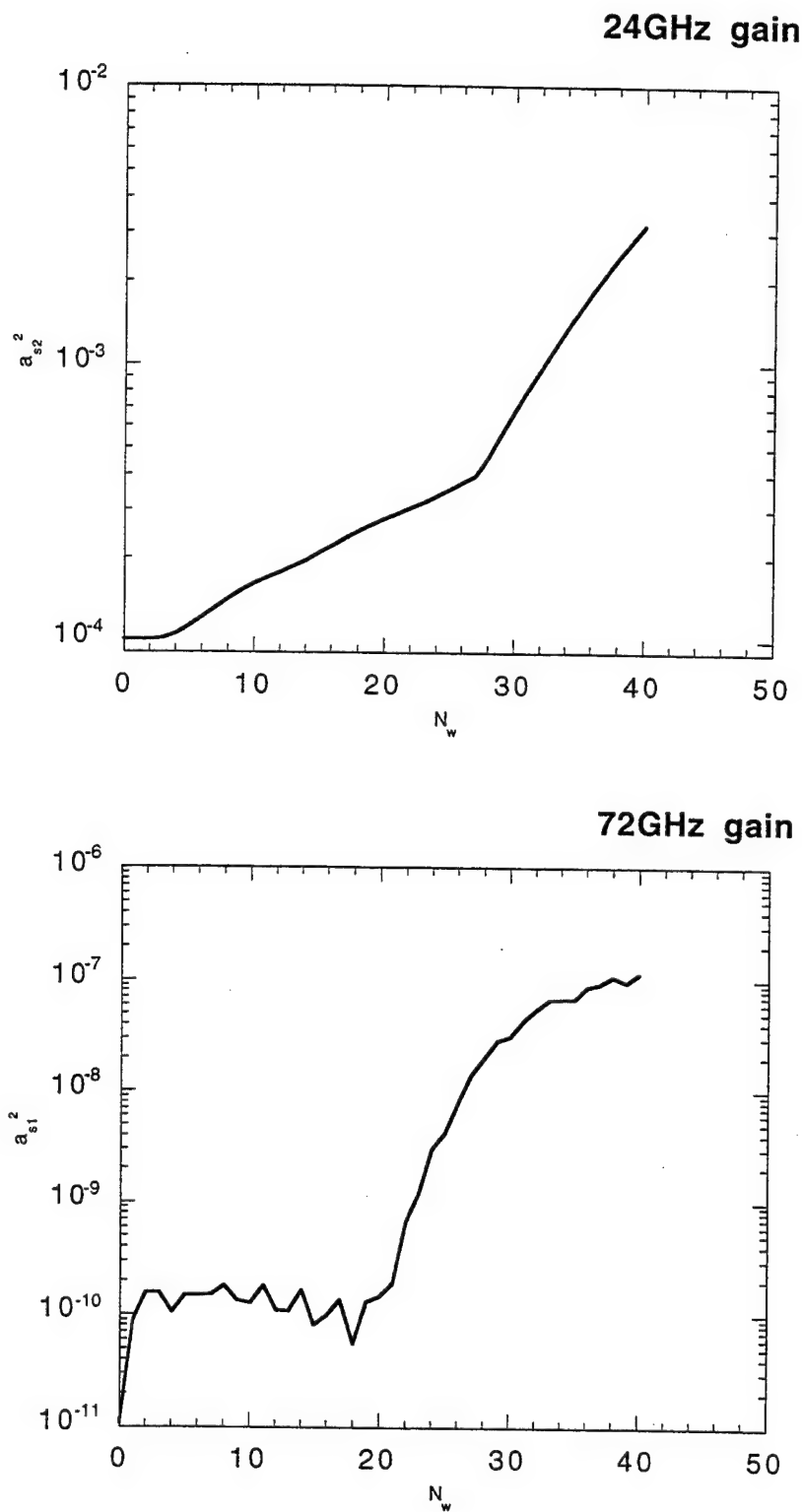


Figure 5.5 The peak power growth of 24GHz (upper) and 72GHz (lower) waves along the undulator with a higher initial signal level at 24GHz.

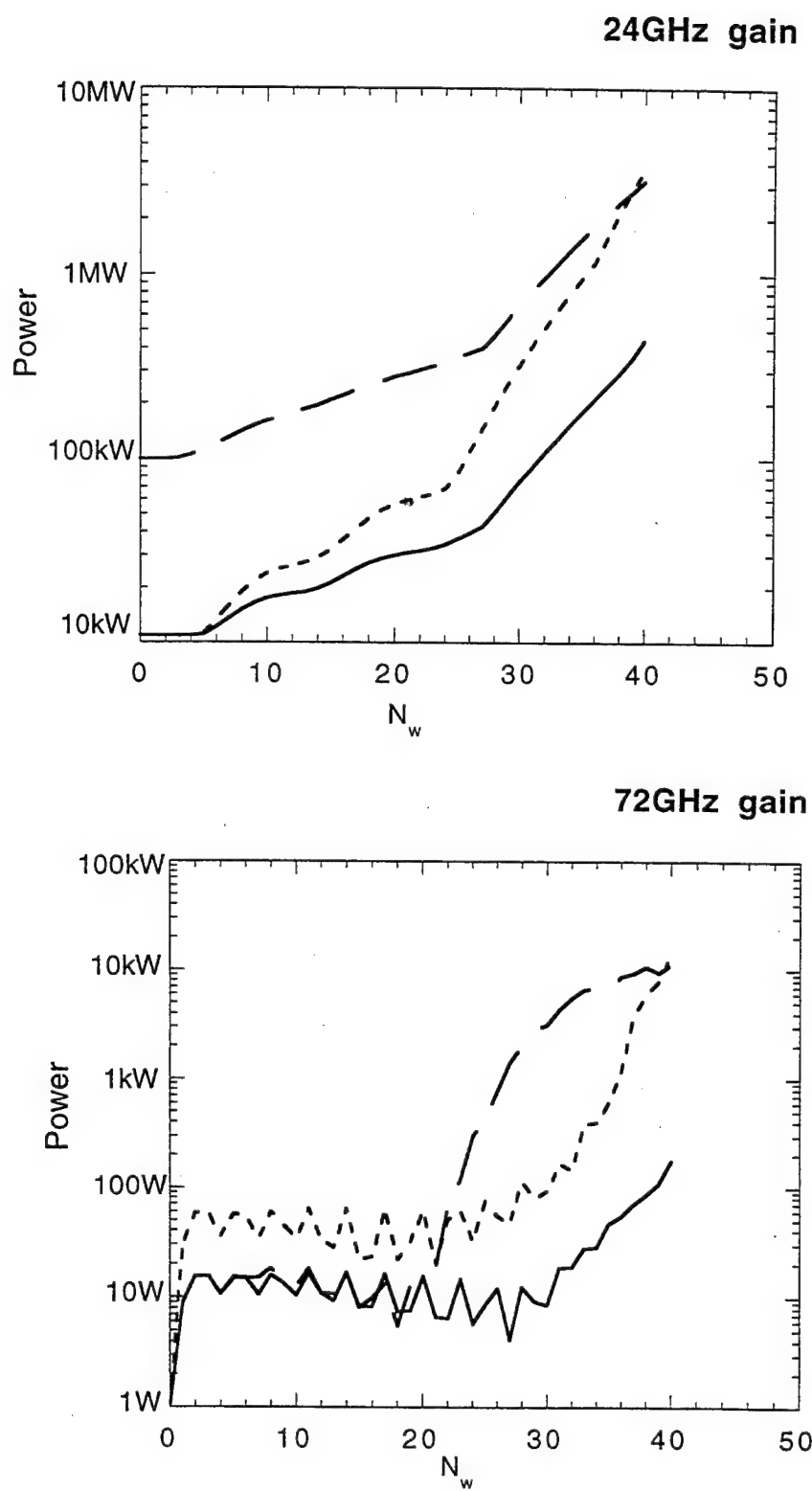


Figure 5.6 The peak power growth of 24GHz (upper) and 72GHz (lower) waves along the undulator in three cases, which are shown by Fig. 5.2, .5.4, 5.5 previously..

5.3 Simulation Results Related to the 7th Harmonic Co-generation

For the 7th harmonic co-generation, we also develop the set of first order partial differential equations (Eq. 2.44-2.47). By doing the same variable transformation in section 5.1, we can get the same set of equations (Eq. 5.2-5.5) with $\alpha = 7$. Then we can use the same technique to numerically solve these equations.

Fig. 5.7 is an example we calculated that is relevant to the seventh harmonic experiment. It shows the peak power growth of the 24GHz and 168GHz along the undulator. The 24GHz wave starts from an initial signal of 10kW ($a_{s2}^2(0) = 10^{-5}$) in the right circular "rotating" mode, and develops a power gain of 100 at the end of the undulator. The 168GHz grows from a low signal level. In this simulation run, the two waves travel at the same speed (the group velocity is about $0.5c$ in the waveguide), i.e. there is a perfect group velocity matching between these two waves. Since $v_{g1} = v_{g2}$, the term containing the x derivative in Eq. (5.4) vanishes, so the two waves both move along the y direction, and no interpolation is needed for this computation.

In reality, the 7th harmonic doesn't travel with the exact same speed with the fundamental mode. Based on Fig. 2.2, there is a $\sim 1\%$ mismatch ($v_{g1} \approx 0.99v_{g2}$) between the group velocities of the 7th harmonic $TE_{7,2}$ mode and the fundamental TE_{11} mode. In order to simulate this 1% group velocity mismatch, we need to use the interpolation method as we did for the third harmonic cases, since this time the 7th harmonic travels along its characteristic line, instead of the y direction. Fig. 5.8 shows this 1% mismatch case, the 0% mismatch case results are also shown in the same figure for comparison. As expected, the 168GHz wave grows differently in two cases because of the mismatch in velocity, especially in the first 25 wiggler periods. When the spatial growth rate gets bigger than the wavenumber mismatch (0.7cm^{-1}), the rapid growth will compensate the phase mismatch, which is possibly why the difference between the two cases becomes much smaller after 25

smaller after 25 wiggler periods. Since the 1% mismatch is more close to the reality, we will use this assumption for the following simulation runs.

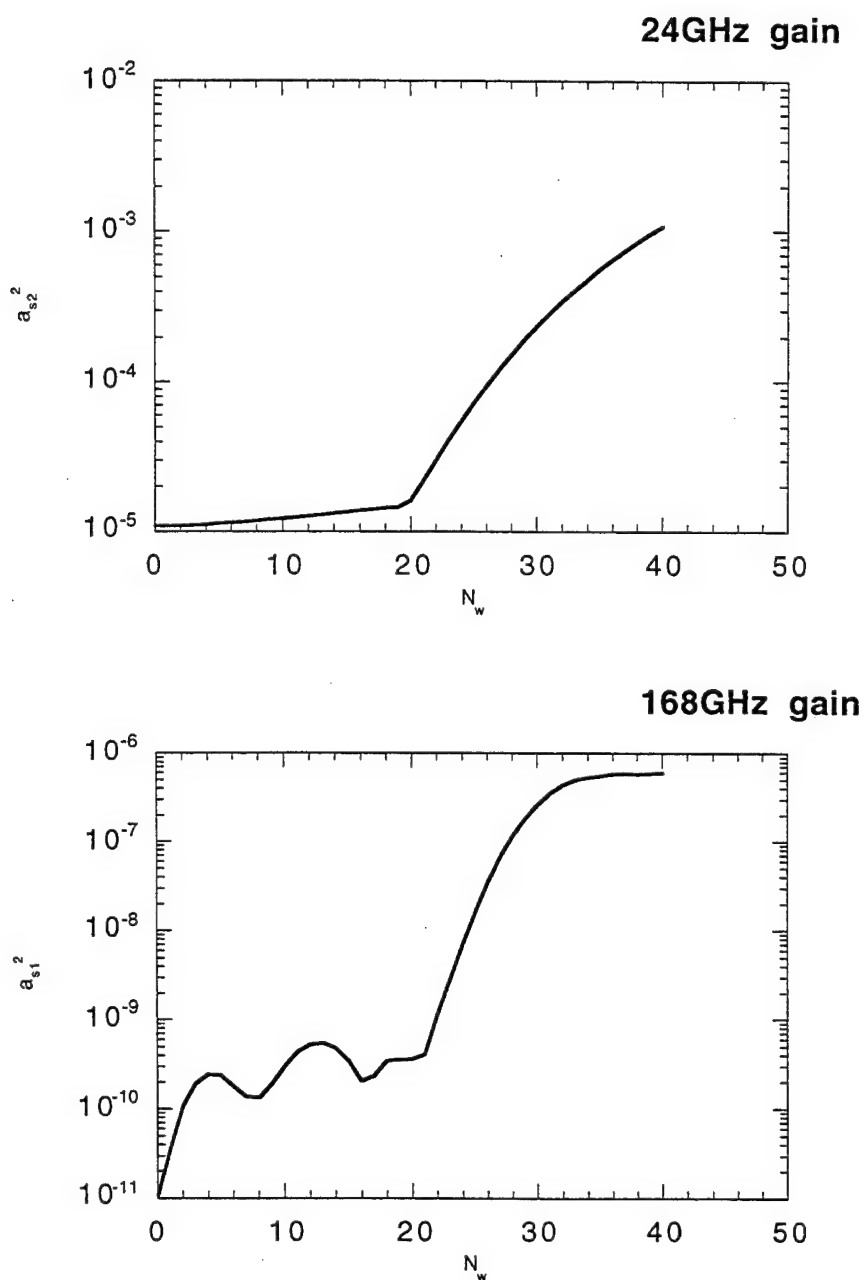


Figure 5.7 The peak power growth of 24GHz (upper) and 168GHz (lower) waves along the undulator; the two waves have perfect group velocity matching.

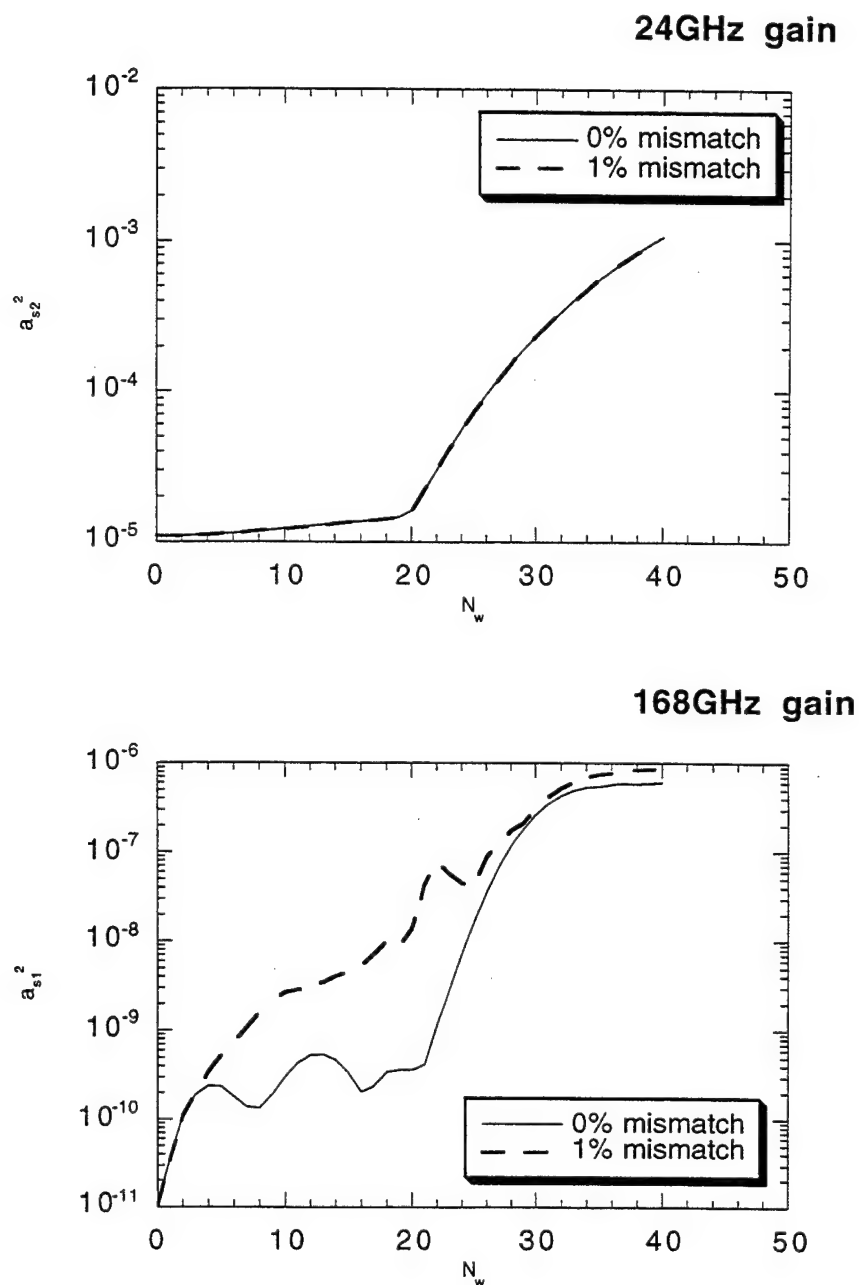


Figure 5.8 The peak power growth of 24GHz (upper) and 168GHz (lower) waves along the undulator in two cases: 0% mismatch case and 1% mismatch case.

As we did in the third harmonic case, in order to make the microwave output near saturation, we start the 24GHz wave from a higher initial signal level of 100kW instead of 10kW. Fig. 5.9 is the simulation results for this case (the solid line pair). As shown in the

figure, if the FEL output is driven near saturation ($\sim 2\text{MW}$), the conversion of microwave power to the 7th harmonic is nearly 30% when the signals reach the end of the undulator, which is much bigger than 7% in the 10kW case (the broken line pair).

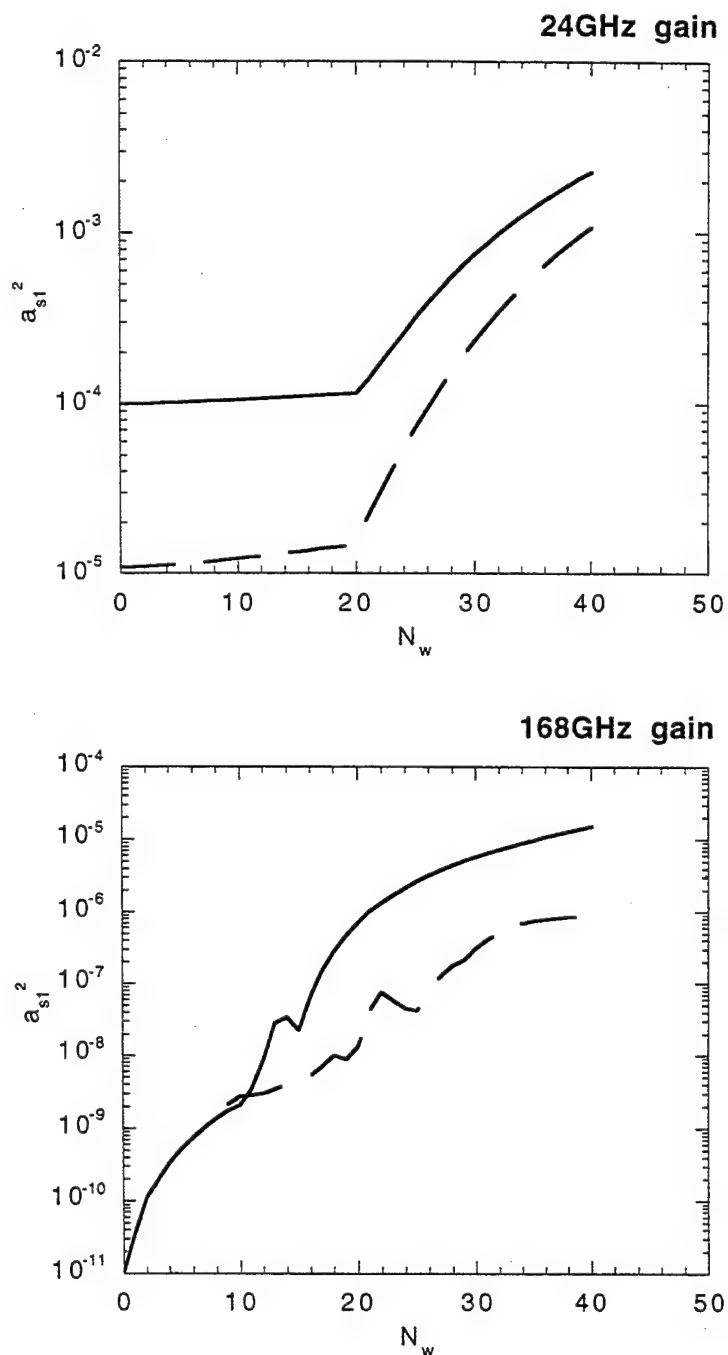


Figure 5.9 The peak power growth of 24GHz (upper) and 168GHz (lower) waves along the undulator, with 10kW (broken line) and 100kW (solid line) 24GHz input power.

In order to understand how the bunching current drive the two waves, we present the Fig. 5.10 to show the harmonic components of the electron bunching (upper) and the corresponding gain profile (lower).

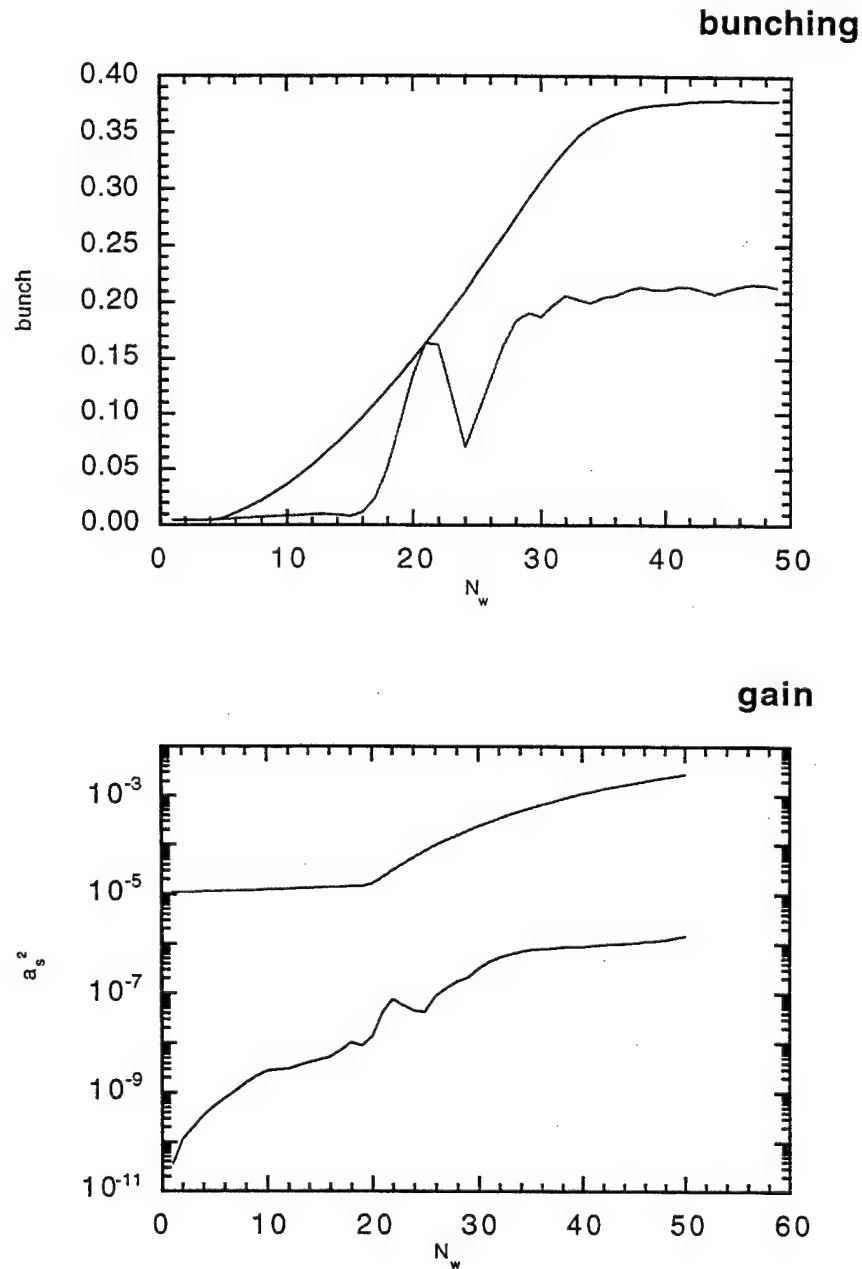


Figure 5.10 The power growth of 24Ghz (upper) and 168Ghz (lower) along the undulator in the gain figure, driven by the bunching current $\langle e^{i\theta} \rangle$ (upper) and $\langle e^{i7\theta} \rangle$ (lower) in the bunching figure .

We need to point out that all these results shown (Fig. 5.7-5.11) are 1D simulations and the overlap between the particles and the two different radiation modes ($TE_{7,2}$ and TE_{11}) are being modeled with the same filling factor 0.07, which is chosen to get approximately the same power gain at 24GHz as we observed in the experiment.. Since a 3D simulation is really necessary to model the off-axis behavior of the beam and its overlap with the waveguide mode, the results of all those simulations cannot be compared with the experiment quantitatively, but may serve as an incentive for further study. Indeed, a 3D code [3] has been used recently to model the generation of the seventh harmonic signal. Appreciable seventh harmonic output (~2kW) has been found [4] using the Raman version of this code with the electron beam located off-axis; much smaller power (~ 200W) was found when the beam was located on-axis. These results, which are not much different from our experimental findings, will be presented in more detail elsewhere, as the optimum location of the electron beam for power conversion has yet to be found.

5.4 The Single-Frequency Code

We presented two figures (Fig. 4.2, 4.10) in Chapter 4 to show the computed gain spectrum of the waveguide FEL using a so called "single-frequency" code. We will introduce this code in this section.

Basically the single-frequency code is used to solve the equation set Eq. 2.18-2.20, in which there is only one wave interacting with the electron beam. Since we simulate the same system (the Columbia FEL facility), we need to use the same set of operation parameters, such as the electron beam energy, wiggler period and so on, i.e. the same condition under which the 24GHz and 72GHz are resonant. Due to this reason, we obtain the single-frequency code by modifying our 2-wave simulation code.

We still use ω_2 representing the 24GHz wave, ω_1 representing the interacting wave, with $\omega_1 = \alpha\omega_2$, but this time α can be a real number instead of an integer. We

know, $\theta_1 = k_w z + k_1 z - \omega_1 t$ and $\theta_2 = k_w z + k_2 z - \omega_2 t$, based on this two formula, we can get:

$$\theta_1 = \theta_2 + (k_1 - k_2)z - (\alpha - 1)\omega_2 t \quad (5.7)$$

then

$$\left(\frac{\partial}{\partial z} + \frac{1}{v_1} \frac{\partial}{\partial t} \right) \theta_{1j} = \left(\frac{\partial}{\partial z} + \frac{1}{v_1} \frac{\partial}{\partial t} \right) \theta_{2j} + (k_1 - k_2)z - \frac{(\alpha - 1)}{v_1} \omega_2$$

since $\left(\frac{\partial}{\partial z} + \frac{1}{v_1} \frac{\partial}{\partial t} \right) \theta_{2j} = \overline{k_{w2}} \left(1 - \frac{\overline{\gamma_{r2}^2}}{\gamma_j^2} \right)$ (Eq.2.29), and $\omega_2 = v_1(k_w + k_2)$ (Eq. 2.21), we

obtain the phase equation related to ω_1 :

$$\left(\frac{\partial}{\partial z} + \frac{1}{v_1} \frac{\partial}{\partial t} \right) \theta_{1j} = \overline{k_{w2}} \left(1 - \frac{\overline{\gamma_{r2}^2}}{\gamma_j^2} \right) + (k_1 - k_2)z - (\alpha - 1)(k_w + k_2) \quad (5.8)$$

The electron energy equation and the wave equation should be the same as Eq.2.19,

2.20:

$$\left(\frac{\partial}{\partial z} + \frac{1}{v_1} \frac{\partial}{\partial t} \right) \gamma_j = -\frac{a_w}{\gamma_j v_{1j}} a_{s1} \omega_1 \sin \psi_{1j} \quad (5.9)$$

$$\left(\frac{\partial}{\partial z} + \frac{1}{v_{s1}} \frac{\partial}{\partial t} \right) a_1 = i \frac{\overline{\omega_p^2} a_w}{2c^2 k_1} \left\langle \frac{e^{-i\alpha\theta_1}}{\gamma} \right\rangle \quad (5.10)$$

The computational code which integrates this complete set of equations (Eq. 5.8-5.10) is called the "single-frequency" code; in the simulation, we used the same variable transformation and same numerical method as we did for the two-wave model. By computing the power gain at different frequencies for electron beam energy of 600kV and 400kV, we can get the two figures, Fig. 4.2 and Fig. 4.10.

Reference:

- [1] William H. Press et al, Numerical Recipe (in C), p589, Cambridge University Press.
- [2] Y._P. Chou and T.C. Marshall, Nucl. Instrum. Meth. in Phys. Res. **A318**, p528 (1992).
- [3] H.P. Freund and T.M. Antonsen, Jr., "Principles of Free Electron Lasers", Chapter 5, second edition, Chapman and Hall, London (1996).
- [4] H.P. Freund, private communication.

Chapter 6

Conclusion

Millimeter harmonic emissions have been observed in our experiment and compared with numerical simulations based on our 1D FEL theory. We believe this harmonic output power can be of use to create coherent, phase-referenced power in the millimeter spectrum for applications such as pulse radar and accelerator physics.

We use a 10kW 24GHz microwave signal as the fundamental mode to prebunch the 600kV electron beam, and up to 400kW 24GHz signal is obtained from the Columbia FEL facility in the TE_{11} mode of a cylindrical waveguide. The FEL operates as a single-pass traveling wave amplifier instead of an oscillator, so the output should be stable and free of sidebands. We choose the parameters of the experiment so that both the fundamental (24GHz) and its third harmonic (72GHz) are resonant FEL interactions in a cylindrical waveguide. A few hundred watts of 72GHz signal are emitted, most likely in the TE_{11} mode, accompanied by even smaller second harmonic. We found substantial (a few kW) emission at the seventh harmonic (168GHz), most likely from the TE_{72} mode, by displacing the electron beam from the system axis, about 2mm in our experiment. The third harmonic radiation does not compete with the seventh for the free energy of the bunching, because the seventh harmonic power is nearly zero when the electron beam is positioned on the axis.

We also obtained the seventh harmonic output when the electron beam energy is as low as 400kV; this represents the "tangent" FEL waveguide case, in which there is only one FEL resonant mode. This represents a very convenient way to generate appreciable 2mm wavelength power, using a FEL operating at comparatively low beam energy driven

by a powerful microwave source, for the purpose of plasma electron cyclotron resonant heating.

We mixed the frequency-tripled 24GHz power ($\sim 100\text{mW}$) with the 72GHz third harmonic power from the FEL and obtained a signal, which shows that the millimeter third harmonic radiation is coherent and phase-related to the fundamental radiation. This feature makes our harmonic output more useful for applications where this is necessary, e.g., rf for accelerators and pulse radar.

The theoretical study of the harmonic radiation is based on numerically solving a complete set of FEL equations that govern the dynamics of the two harmonically related radiation waves and the electron motion in an FEL. These equations are derived for a cylindrically symmetric waveguide FEL, which are first-order 1D partial differential equations. The computational parameters (to simulate our Columbia FEL) are chosen so as to make the third harmonic and the fundamental the two resonant modes (in TE_{11} mode) of the waveguide FEL. Detailed numerical studies show that about a few hundred watts of the third harmonic (72GHz) emission is obtained along with the amplified (gain of 40) 24GHz prebunching wave. These computational results are quantitatively consistent with the experimental results. The computations also show that, by increasing the input signal of the microwave, we can get more harmonic radiation.

Based on the 1D theory derived for the seventh harmonic co-generation, the computations show that there is seventh harmonic (168GHz in the TE_{72} mode) generation from the Columbia FEL, when there is gain at the fundamental mode (24GHz in the TE_{11} mode), since the two waves travel at nearly the same speed in the cylindrical waveguide. The computed gain spectrum shows that there is gain at 24GHz both when the electron beam energy is 600kV and 400kV, which explains the experiments where we observed the seventh harmonic emission in the above two cases. Even though a 3D model is really necessary to simulate the off-axis behavior of the electron beam and its overlap with the waveguide mode, the simulations we did can serve as an incentive for further study.

Indeed, 3D code simulation results done elsewhere have indicated seventh harmonic power output consistent with our experimental results.

This is the first time that seventh harmonic power has been obtained from a free electron laser. Although the power output of the harmonics in this experiment is not large, the numerical result shows that more powerful radiation can result if the driving power at the microwave frequency is increased. Maintaining modest gain and the traveling-wave operation will assure good frequency quality for the harmonic radiation.